HHS Public Access

Author manuscript

Cell Rep. Author manuscript; available in PMC 2022 August 22.

Published in final edited form as:

Cell Rep. 2022 July 26; 40(4): 111139. doi:10.1016/j.celrep.2022.111139.

Dynamic control of visually guided locomotion through corticosubthalamic projections

Elie M. Adam[1,3,*], **Taylor Johns**[1], **Mriganka Sur**[1,2,*]

[1]Picower Institute for Learning and Memory, Massachusetts Institute of Technology, Cambridge, MA 02139, USA

[2]Department of Brain and Cognitive Sciences, Massachusetts Institute of Technology, Cambridge, MA 02139, USA

[3]Lead contact

SUMMARY

Goal-directed locomotion requires control signals that propagate from higher order areas to regulate spinal mechanisms. The corticosubthalamic hyperdirect pathway offers a short route for cortical information to reach locomotor centers in the brainstem. We developed a task in which head-fixed mice run to a visual landmark and then stop and wait to collect the reward and examined the role of secondary motor cortex (M2) projections to the subthalamic nucleus (STN) in controlling locomotion. Our behavioral modeling, calcium imaging, and optogenetics manipulation results suggest that the M2-STN pathway can be recruited during visually guided locomotion to rapidly and precisely control the pedunculopontine nucleus (PPN) of the mesencephalic locomotor region through the basal ganglia. By capturing the physiological dynamics through a feedback control model and analyzing neuronal signals in M2, PPN, and STN, we find that the corticosubthalamic projections potentially control PPN activity by differentiating an M2 error signal to ensure fast input-output dynamics.

Graphical abstract

*Correspondence: eadam@mit.edu (E.M.A.), msur@mit.edu (M.S.).

AUTHOR CONTRIBUTIONS

E.M.A. and M.S. conceived the project and developed the concepts presented. E.M.A. designed the experiments and performed them with assistance from T.J. in behavioral training and animal care. E.M.A. analyzed the data and developed the theory. E.M.A. and M.S. wrote the manuscript, with input from T.J.

DECLARATION OF INTERESTS

The authors declare no competing interests.

SUPPORTING CITATIONS

Alexander et al. (1986); Barthas and Kwan (2017); Bertsekas (1995); Esposito and Arber (2016); Hintiryan et al. (2016); Hooks et al. (2018); Mandelbaum et al. (2019); Shik et al. (1969); Swann et al. (2012); Whelan (1996); Yamawaki et al. (2016); Zhang et al. (2014); Zhang et al. (2016).

SUPPLEMENTAL INFORMATION

Supplemental information can be found online at https://doi.org/10.1016/j.celrep.2022.111139.

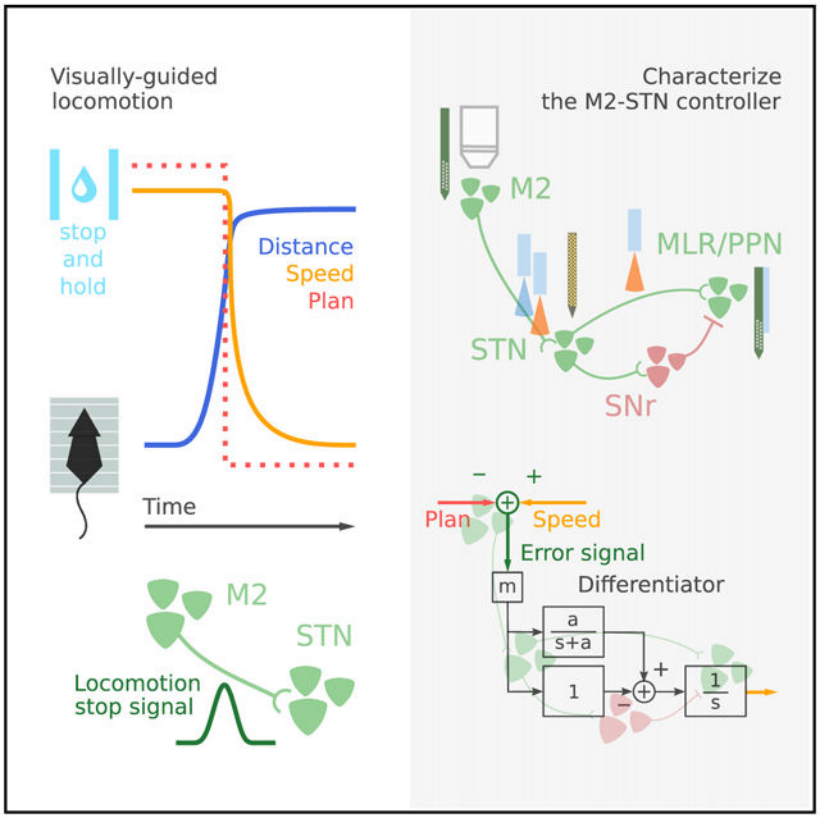

In brief

Using a combination of optogenetics, 2-photon imaging, extracellular recordings, and control theoretic models in behaving mice, Adam et al. find that the M2-STN projection sends stop signals to halt visually guided locomotion and potentially controls the MLR/PPN through SNr by differentiating an M2 error signal for the rapid control of locomotion.

INTRODUCTION

Coordinated movement, and in particular, locomotion, is enabled by distributed spinal and brain circuits. Although the executive mechanisms for locomotion are implemented in the spinal cord (Goulding, 2009; Grillner, 2003; Kiehn, 2006, 2016), locomotion is importantly regulated by supraspinal circuitry (Ferreira-Pinto et al., 2018; Kim et al., 2017; Ryczko and Dubuc, 2013). Brainstem circuits can induce locomotion upon targeted stimulation (Caggiano et al., 2018; Capelli et al., 2017; Josset et al., 2018; Roseberry et al., 2016); however, goal-directed locomotion, especially when guided by sensory information, requires control signals from higher order areas directed toward the spinal cord (Arber and Costa, 2018; Drew et al., 2004; Grillner et al., 2008). The repertoire of higher order signals required to regulate locomotion, and the neural circuitry that enables such signaling, are particularly unclear in behavioral settings (Arber and Costa, 2018). The control principles and substrates governing action can further suggest principles for cognitive control, particularly if the same neural substrate supports multiple functions.

While the regulation of locomotion is mainly implemented in the brainstem, movement planning is considered to arise at the level of the cortex (Churchland et al., 2010; Economo et al., 2018; Shenoy et al., 2013; Svoboda and Li, 2018; Wong et al., 2015). The basal ganglia are situated between these two centers and importantly regulate voluntary movement (Bolam et al., 2000; Graybiel, 2000). The direct and indirect pathways, initiated from the striatum, bidirectionally control locomotion (Roseberry et al., 2016) through the *substantia nigra pars reticulata* (SNr) and its control over the mesencephalic locomotor region (MLR) (Freeze et al., 2013; Liu et al., 2018). The basal ganglia additionally admit a cortical input straight to the subthalamic nucleus (STN) (Nambu et al., 2000, 2002), which projects to SNr (Hamani et al., 2004). This pathway has been called the hyperdirect pathway, and evidence across species, notably humans, has shown stop activity at the source of this pathway in reactive stop-signal or go/no-go tasks (Aron et al., 2016; Aron and Poldrack, 2006; Eagle et al., 2008; Wessel and Aron, 2017; Chen et al., 2020). The STN itself is considered pivotal in stopping movement (Hamani et al., 2004; Schmidt et al., 2013). In rodents, reducing the excitatory output of STN induces hyperlocomotion (Schweizer et al., 2014), and lesions of STN induce impulsive responding (Baunez and Robbins, 1997; Eagle et al., 2008; Uslaner and Robinson, 2006). More recently, optogenetic studies in mice show that areal activation of STN excitatory cells disrupts self-initiated bouts of licking (Fife et al., 2017) and that the activation and inactivation of STN-projecting prefrontal cortex neurons reduced and increased inappropriate licking (Li et al., 2020). Bilateral optogenetic inhibition and activation of STN has also been shown to increase and decrease locomotion, respectively (Guillaumin et al., 2021), and such effects can be mediated by certain molecularly defined subpopulations of STN neurons (Parolari et al., 2021). Thus, the hyperdirect pathway stands as an important short-latency cortico-brainstem route for fast control of locomotion.

Goal-directed locomotion implies a proactive locomotor plan that is implemented to achieve a needed goal. From an engineering standpoint, we can enforce a desired goal trajectory in a system through feedback control (Aström and Murray, 2010). Feedback control is based on an error signal: a measured discrepancy between what we would like the system to do (reference) and what it is actually doing (output). By processing such a signal through a controller and feeding it to the system (plant) we intend to control, we ensure adequate performance (Dahleh et al., 2004; Oppenheim et al., 1996). If such a principle is implemented in neural circuits, then we would expect surges in neural signals upon sudden changes in planned locomotion trajectories, and such signals would drive movement corrections to ensure fast control.

We thus developed a task in which head-fixed mice run to a visual landmark, then stop and wait to collect the reward, and examined the projections from the secondary motor cortex (M2) to STN. We hypothesized that these projections send rapid signals that halt locomotion. Here, we report the existence of such signals sent from M2 to STN that halt visually guided locomotion. This positions the hyperdirect pathway as a controller onto the MLR, and particularly its pedunculopontine nucleus (PPN), in the midbrain. Furthermore, using dynamical systems and control engineering methods, we find that the hyperdirect pathway potentially controls the MLR/PPN by differentiating an M2 error signal to ensure fast input-output dynamics.

RESULTS

Mice were trained to run, stop, and wait at visual landmarks to collect reward

We developed a task that allowed us to examine proactive visually guided locomotion stops (Figure 1A). A head-fixed mouse was positioned on a self-propelled treadmill in a virtual runway flanked on both sides by a continuous streak of light-emitting diodes (LEDs). At the start of a trial, the animal was presented with a visual landmark consisting of a lit contiguous subset of LEDs, at a variable position from the animal. The movement of the treadmill was coupled to the movement of the landmark; as the mouse rotated the treadmill to move forward, the landmark approached the mouse. The mouse was then required to run and stop at the landmark, holding its position for 1.5 s to collect the reward. If the mouse waited at the landmark for the required time, then it received a reward tone and a water reward simultaneously. If the mouse either ran to the end of the runway, bypassing the landmark, or failed to stop at the landmark within 30 s, then it received a miss tone. After the reward or miss tone, all of the LEDs were turned off and a new trial started after 1 s, with a landmark reappearing (Video S1).

We ensured that the distance over which the landmark position randomly varied was greater than the width of the landmark. This prevented the animal from relying on tracking the distance to the landmark internally, ensuring that the task was indeed visually guided (Figures 1B, S1A, and S1B). The task elicited an on-off locomotion pattern (Figures 1C and S1A), and we carefully examined the stops. Furthermore, this pattern was a learned behavior (Figures S1F–S1I) as evidenced by the increase in stop-wait time as training sessions progressed (Figure S1F) and an increase in hit rates in a simpler version of the task during the first stages of training in which landmarks were not present (Figure S1G). Our task was designed to elicit short bouts of runs and stops, instead of lengthy periods of locomotion (STAR Methods). Our task design was intended to elicit locomotion in the “moderate velocity” regime (as opposed to high velocity behaviors such as escape behavior) with the goal of engaging PPN in the MLR, and more likely basal ganglia circuitry, instead of the cuneiform nucleus (Caggiano et al., 2018; Josset et al., 2018). Importantly, the trajectory of the speed signal was not affected by the distance of the landmark (Figure S1J) if kept in close range. In all subsequent experiments, the trajectory of the stop was preserved throughout (Figure S1K).

The behavior suggests a sudden switch in locomotion state

We modeled the behavior of the animal in a single trial as an optimal-control problem (Figure 2A; Methods S1A). Starting from an initial position away from the landmark, the mouse was tasked to select a locomotor plan that dictates its locomotion pattern so as to minimize time to collect the reward, thereby maximizing the reward in a session. We then solved this control problem for the optimal solution via Lagrangian methods (Methods S1A) and found it to be a bang-bang control policy, in which the locomotion plan abruptly switches from a maximum value to a minimum value. Therefore, to collect the reward as soon as possible, the animal should accelerate as much as possible up to a switching point, which likely occurs before the animal arrives at the landmark, then suddenly brake as much as possible to arrive at a full halt at the landmark. This model yields two features. First,

the optimal solution suggests that there is an essential switching point in behavior: if the brain generates a signal to stop, then it should occur around this switching point. Second, the model depends on a time constant and by changing its value, we can modulate how quickly the animal stops. Signatures of these strategies were later analyzed in the neurophysiological recordings.

From each session, we recovered time windows around all of the stops at the landmark, which we called landmark-stop windows, and we let the switching point in each correspond to the time point at which the speed of the animal last peaked before stopping. We then aligned all of the speed trajectories in the time windows along their switching point (Figure 2B). The model fitted well to the average trajectory with an average time constant τ of 63.75 ms (Figures 2C and S1C–S1E; STAR Methods). Importantly, having a small enough τ was essential for the animal to stop in a timely manner at the landmark. For instance, if τ were equal to 1 s, then the animal would not stop in time and would miss the landmark (Figure 2C). (The velocity fluctuated while the animals were running, and we refer the reader to Methods S1A for a discussion of the model.)

Activating M2 axons in STN leads to stopping

Our behavioral model indicates a switching point in behavior and suggests that the brain generates a signal at that time. We hypothesized that the M2-STN pathway may be sending a signal to achieve rapid locomotion stops (see Methods S1B). Thus, we asked: If activity is sent along the M2-STN pathway, does it then lead the animal to stop locomoting?

To address this question, we injected an adeno-associated virus (AAV) expressing channelrhodopsin-2 (ChR2) under the Ca^{2+}/calmodulin-dependent protein kinase II (CaMKII) promoter in M2, and implanted an optic fiber above ipsilateral STN to target the M2 axons there (Figures 3A and 3B). On a random subset of trials, we delivered a brief burst of blue (473 nm) light (at 20 Hz for 500 ms) into the optic fiber to activate the axons once the animal crossed the middle of the runway, while running toward the landmark (Figure 3A). We found that activating the axons led the animal to stop prematurely (Figures 3C–3F). This suggests that if the brain transmits a signal along the hyperdirect pathway right before stopping, then it will causally trigger the animal to stop. However, the optogenetic activation was not effective at inducing premature stopping in all of the trials (Figure 3F), likely due to its being unilateral and to the presence of redundant circuits whose activity alteration may be necessary to initiate stopping. To verify that this effect was not due to inadvertently activating fibers beneath STN in the cerebral peduncle (and not only M2 boutons in STN) because of spurious laser effects reaching that area, we instead targeted the M2 efferents anterior to the STN by placing the optic fiber above the cerebral peduncle. We found that stimulation did not affect locomotion (Figures S2A–S2C). Furthermore, when we injected an AAV expressing only GFP (Figures S2D and S2E) and placed an optic fiber above STN, we found no premature stopping during the optogenetics control experiment upon laser delivery (Figure S2F).

Stop activity is seen in M2-STN neurons on landmark stops but not mid-stops

We next asked: Is there activity at the onset of stopping in the M2-STN pathway? To answer this, we imaged the calcium activity (GCaMP6f) of M2 neurons projecting to STN using two-photon microscopy. For each imaged neuron, we retrieved the activity during the landmark-stop windows (1 s before the switching point and 1.5 s after), averaged it across these windows, and found a range of responses in different epochs (Figure 4A).

For a principled clustering, we derived a low dimensional subspace, which explained more than 80% of the energy in the neural population response (Figures 4B, S3A, and S3B). Through a change of basis, each neuronal response corresponded to a weighted combination of three basis functions (Figures 4C, S3A, and S3B), representing ideal pre-stop, stop, and post-stop neurons, with an additional noise term (STAR Methods). We used the weights to cluster the neurons into three groups and recovered a fraction that is active during stops (Figure 4D), which showed significantly more reliable responses to stopping compared to the other two groups (Figure 4E). We then collected activity during spontaneous stops performed by the animal as it ran toward the landmark. We aligned the activity to switching points in spontaneous-stop windows (as done for landmark-stop windows) and averaged it across windows for stop neurons. We found that M2 neurons are significantly more active at stops at the landmark that are visually guided compared to spontaneous stops in the middle of the track (paired t test, $p = 1.09e{-}6$) (Figures 4F–4H and S4A–S4C), indicating that during task performance, M2 neurons specifically signal goal-directed visually guided stops.

Our imaging results revealed a surge of activity at the onset of the visually guided stop, and our axonal activation results showed that such a surge can halt locomotion. To assess whether such an activity surge is necessary, we expressed halorhodopsin from *Natronomonas* (NpHR) bilaterally in M2, and implanted two optic fibers bilaterally over STN to target the M2 axons there (Figures 4I and 4J). On a random subset of trials, we delivered continuous amber (589 nm) light to inhibit the axons when the animal approached the landmark. We found that inactivation increased the number of misses (Figure 4K), while light delivery in control experiments (Figures 4K, S2D, S2E, S2G, and S2H) did not. However, the effects of inhibition appeared weak. Indeed, it can be unclear how effective axonal inhibition using NpHR is in our setting. In addition, the indirect pathway of the basal ganglia receives cortical input and promotes stopping via STN; it can also provide redundant information to supplement the signals sent through the corticosubthalamic projection. Furthermore, mice appear to exhibit a higher miss rate during laser off trials compared to controls (Figure 4K). It may be the case that the effect of stimulation disrupts regular basal ganglia neuronal rhythms and may have repercussion on future trials;its effect may not be confined to laser on trials leading to overall more misses.

With the existence of the surge of activity established, the question we then asked was: How does that surge of activity drive locomotion to halt?

Behavioral dynamics can be physiologically realized through feedback control

We next sought a physiological realization of the behavioral model that connects the physiology and anatomy to the braking dynamics as depicted by our behavioral model.

We modeled the physiological dynamics through a feedback control system, whereby the neural circuitry tracks a neuronal reference signal depicting the locomotion plan and ensures a quick reaction in velocity at the onset of stopping (Figures 5A and 5B).

Our model proposes that the M2-STN projection controls the MLR, particularly its PPN), through the SNr (Figure 5A) (see Methods S1C for modeling details and rationale). Our model also proposes M2 as computing a discrepancy between a locomotion plan and the current locomotion state of the animal (Figure 5B; Methods S1C). At the switching point, derived from the behavioral model (Figure 2A), the discrepancy is significant, leading to "error signals" that are sent down along the M2-STN projections. These error signals had appeared in the form of stop signals, notably in the imaged responses. Signals of a possibly similar nature have been reported in frontal cortices, to report visuomotor mismatch, in the context of predictive coding (Attinger et al., 2017; Heindorf et al., 2018). Since we defined the PPN as integrating neuronal input to drive locomotion (Methods S1C), feeding these error signals directly to PPN would correct its response and allow a decrease in velocity. Crucially, however, if these error signals were directly fed into PPN as a control mechanism, then the animal would not be able to stop quickly enough to collect the reward. Indeed, the behavioral model has the parameter τ, which is required to be small enough for locomotion halts to be rapid. We propose that the controller needs to overcome the slowness limitation by performing a mathematical differentiation operation, thereby canceling out the slow integrative dynamics of PPN. Anatomically, STN projects to PPN via two pathways, one inhibitory and one excitatory, whose precise temporal interaction can simulate differentiation, yielding the necessary computation to drive rapid dynamics (Figures 5A and 5B). To fully characterize the controller, we require three kinds of information—on the input space, the input-output relation, and the dynamical state of the controller. The physiological experiments that follow are designed to provide this information (Figures S5A–S5C).

We purposefully kept the model simple to focus it on a key point: capturing the speed of stopping through a time constant. The main prediction of the model is the necessity of a controller that performs differentiation (essentially a high-pass filter) of the M2 stop signals; without such a controller, we cannot attain an adequate time constant. The next experiments are designed to examine this point.

Fast input-output dynamics are enabled by mathematical differentiation

To study the input-output relation and the characteristics required by a controller to achieve rapid locomotion halts, we recorded single-unit extracellular activity in M2 and MLR/PPN simultaneously using silicon probes. We gain the temporal resolution necessary to analyze input-ouput and decay dynamics by transitioning from 2-photon imaging to extracellular recordings. While we lose the cell specificity by doing so, we recover it through additional opto-tagging experiments.

For each recorded unit, we retrieved the spiking activity during the landmark-stop windows, averaged all of the activity, then smoothed it to obtain average firing rates (STAR Methods). Sorting the average responses revealed a heterogeneity in the types of neural responses in both M2 and PPN (Figure 6A), similar to that observed by calcium imaging of M2 responses

(Figure 4A). We then performed a principled clustering of neuronal responses, as performed for the imaged responses (Figures 4B and 4C), and similarly recovered three groups of neurons, revealing a fraction that are active during stops (Figures 6B and 6C). Both brain structures are considered to be implicated in the task and admit such stop neurons; however, the fraction of stop neurons is significantly higher in M2 (51/126 in M2 versus 17/141 in PPN; chisquare test p = 3.5e−14), indicating that these signals are not equally widespread throughout the brain (Figure 6C). Furthermore, each group of neurons was found to respond more reliably within its corresponding epoch, when compared to the other groups (Figure 6D). To verify that the velocity and the corresponding neural activity do not produce time lags or decay at different rates, we recovered neural activity in PPN that reflects locomotion speed (STAR Methods) and compared it to the decay in speed. We observed that the activity is linearly related (up to baseline offset), thereby incurring no change in decay rates (linear regression during the second after onset of stopping, $R^2 = 0.829$ p = 5.36e−78) (Figure 6E). This implies that we can study the average rate of decay in velocity during stopping by studying the average rate of decay in neural activity during stopping.

The PPN, however, has a number of cell types, with different, potentially opposing functions (Caggiano et al., 2018; Josset et al., 2018). Thus, we next investigated the roles of excitatory and inhibitory cells in the PPN in the context of the task using optotagging. We expressed ChR2 in a Cre-dependent manner in PPN of Vglut2-Cre and Vgat-Cre mice to identify excitatory and inhibitory cells, respectively. We lowered a recording probe coupled with an optic fiber and identified the photoresponsive responsive cells (Figures 6F and 6G). The recordings and clustering (Figure 6F) revealed similar activity and proportions obtained in the initial recordings (Figures 6A and 6C). The recordings gathered 36 Vglut2+ units and 26 Vgat+ units (Figure 6I) and showed responses in both pre-stop and post-stop epochs. The reliability of the responses between populations was different: pre-stop Vglut2+ neurons were more reliable in the pre-stop phase than were the post-stop Vglut2+ neurons in the post-stop phase (Figure 6H). The reverse was found to be true for Vgat+ cells. This supports the findings that excitatory cells promote, whereas inhibitory cells suppress, locomotion. To further investigate this, we averaged the trial responses and observed a drastic difference: The response of Vglut2+ cells decayed following the stop, while that of Vgat+ cells increased (Figure 6K). The general pattern of spiking activity of Vglut2+ cells follows that observed in the single unit recordings shown in Figure 6E, and overlaying the plots (after affine transformation to account for differences in firing rates and baseline activity) showed that the two are closely matched (Figure 6L). We refer the reader to Methods S1D for a discussion on how our model fits the cell-type-specific dynamics.

We can derive from our physiological model (Figure 5A) the characterization

$$e(t) = \frac{1}{m}\frac{dy}{dt}(t) + \frac{a}{m}y(t)$$

The error signal consists of a weighted combination of acceleration and velocity (Methods S1C). However, the theoretical error signal around the switching point is negative, as $r(t)$ becomes 0, while $y(t)$ is positive. As neural firing rates are fundamentally non-negative, the error signals sent from M2 to STN can only correspond to $-e(t)$, the negative of the

error term. This, in turn, consists of a weighted combination of a negative acceleration signal $-dy/dt$ and a negative speed signal $-y$ (Methods S1B). We then reconstructed these signal components in M2 (STAR Methods) and reconstructed the input-output relation by identifying the coefficient a (=17.08). Using the reconstructed input-output relation, we derived the predicted PPN response (Figure 6M). Crucially, we constructed an alternative model by removing the differentiation component, leaving only an amplification gain as a means of control. We found that the animal cannot decrease its PPN activity in a timely manner (Figure 6M), suggesting the necessity of a controller performing additional processing to speed up the dynamics (root-mean-square error [RMSE] computed starting from the switching point, $RMSE_{alternate}$-response/$RMSE_{predicted}$-response = 4.45-fold increase).

STN supports the dynamical state required to drive the dynamics

We next performed extracellular single-unit recordings in STN to reconstruct elements of the error signals, the dynamical state, and the differentiation operation (Figures 7A and 7B) (see Methods S1C and S1E for more information). We studied the dynamical state of the controller by linearly decomposing it into two components, as done for the error signal—one component used to differentiate the negative acceleration component and another component used to differentiate the negative speed component (Methods S1C). We first restricted the neuronal population to the neurons in STN, whose firing activity peaked between 250 ms before and 250 ms after the switching point (STAR Methods) (Figure 7C). We considered 250 ms after the switching point as PPN speed activity had reached its minimum at approximately that point (Figure 6D), and we considered 250 ms before the switching point for symmetry and to capture peaks that occur immediately before braking. We found two dimensions in a low-dimensional neural activity space in which the first encodes the negative acceleration and the other encodes its corresponding dynamical state. Crucially, the difference of the activity along these dimensions yields the needed differentiated signal of negative acceleration (Figures 7D and 7E). We repeated the same procedure for the population of neurons in STN, whose firing activity transitioned from low to high after 250 ms (Figure 7F) (STAR Methods), the waiting phase as determined by PPN activity (Figure 6D), and again were able to reconstruct two dimensions that yield the differentiated signal of the negative speed component (Figures 7G and 7H). Combining the sub-spaces for these two populations indicates that the activity in STN can support differentiation. We further find that this activity is characteristic of STN, and is not present in M2 (Figures S6A–S6H) (see Methods S1E for more details).

To verify that these stopping dynamics are indeed related to STN neurons, we photo-identified STN cells by expressing ChR2 in the STN of Vglut2-Cre mice and delivering light while recording (Figures 7I and 7J). Our recordings have identified 20 Vglut2+ cells in 2 mice (Figure 7K), whose activity mostly supports negative acceleration, corresponding to the stop signal (Figures 7L and 7M). This justified studying the unidentified cells in the stopping regime.

Our experiments suggest a role for the STN-PPN projections in interacting with STN-SNr-PPN pathway to accelerate the signals. To test this, we bilaterally injected in the PPN of

Vglut2-Cre mice a retroAAV that expresses the inhibitory opsin Jaws in a Cre-dependent manner (Figure 7N). This causes Jaws to be expressed in STN somas projecting to PPN, among other populations. We then bilaterally implanted optic fibers above STN to target these projection neurons (Figure 7O). In a random subset of trials, we delivered amber light when the animal was approaching the landmark and found that inhibiting these projections led to an increase in miss rate (Figure 7P) as compared to the control group in Figure 4K. This projection is excitatory, and is known to project to excitatory cells in PPN. This is the counterintuitive role in accelerating stopping (rather than promoting locomotion) via its interaction with the STN-SNr-PPN pathway. Regardless, further investigation would be needed to understand the variability in the results of Figure 7P, using a larger number of animals, as well as a more detailed examination of the PPN-projecting STN population—its density, its projection collaterals, and its target location in PPN.

Overall, our results suggest that the STN-PPN and STN-SNr-PPN pathways convey different signals (see, for example, Figures 7D and 7G) whose convergence onto PPN can result in differentiating the M2 error signal. A recent study (Parolari et al., 2021) found STN cells that project either to SNr or to entopeduncular nucleus, but not both. It may similarly be the case that there are two subpopulations of STN cells—one that directly projects to PPN, but not SNr, and another that projects to SNr, but not PPN. Such segregated projection-specific populations may underlie the observed variability in neuronal STN responses and may be the anatomical substrate ensuring that the appropriate locomotion-promoting and -suppressing signals are conveyed to achieve rapid control of locomotion.

DISCUSSION

We have used a simple visually guided locomotion task to derive an important principle of movement control that uses a specific pathway, from M2 to STN, and circuit, from STN to MLR/PPN. Our results demonstrate that a signal is sent down along M2-STN projections to rapidly halt locomotion. Importantly, these signals are visually guided and do not occur during spontaneous locomotion halts. Our results further suggest that the M2-STN-PPN pathway ensures this fast response by differentiating the signal, to compensate for integration dynamics in PPN. In particular, STN activity can reach PPN through SNr, but also through direct STN-PPN projections; the temporal interaction of these two pathways simulates differentiation. Our analysis began by capturing the behavior of the animal through a minimum-time optimal-control problem. This approach captured the rate of stopping through a time constant, and made the notion of switching point central to the analysis. This approach then enabled us to cast the goal of the neural signaling as ensuring a small enough time constant to achieve rapid locomotion halts. We formalized the neural signaling through a feedback control system, and, through a set of experiments, characterized the properties governing the input space, the input-output relation, and the dynamical state of the controller.

Populations of neurons in the brainstem, notably in the medulla, have been found to stop ongoing locomotion (Bouvier et al., 2015; Capelli et al., 2017; Grätsch et al., 2019; Juvin et al., 2016). We expect such reticulospinal cells to be recruited in the context of our task. We do not think that the corticosubthalamic signaling through MLR is bypassing these lower

brainstem circuits, and this warrants detailed future investigations. However, the nature of the locomotion signaling is different. These reticulospinal cells impinge directly onto spinal circuits and offer a low-level direct control of locomotion. The corticosubthalamic signaling necessitates further processing to reach locomotor circuits, and the processing should be designed so that it ensures fast locomotion halts. From an engineering perspective, feedback control can be leveraged to steer the trajectory of a system as needed and ensure desired operation, which in our case consists of additionally ensuring fast responses. This principle is often realized by computing an error signal—reflecting the discrepancy between a reference trajectory and the current trajectory of the system—and using it to oppose the deviation of the system from a desired operation (Aström and Murray, 2010). Our behavioral model implicates a locomotion plan as a reference signal, from which such error signals can be derived. Error signals have been reported widely in the brain. They provide, for instance, a basis for the dopaminergic reward system (Schultz, 1998) and have been instrumental in the control of movement (McNamee and Wolpert, 2019; Shenoy et al., 2013; Wolpert and Ghahramani, 2000), setting a basis for optimal feedback control in motor coordination (Todorov, 2004; Todorov and Jordan, 2002). Error signals necessitate reference trajectories, and such references are often derived from predictive capabilities of brain function. These capabilities have often been formalized through internal models (Huang et al., 2018; McNamee and Wolpert, 2019) and predictive processing (Keller and Mrsic-Flogel, 2018). Indeed, error signals have been especially reported following expectation perturbations, notably visuomotor mismatch (Attinger et al., 2017; Heindorf et al., 2018; Marple-Horvat et al., 1993), as signaling prediction errors. The signals we elucidate could also be of a similar nature. The mechanisms by which they arise are the subject of further research.

Stopping in such a task is typically considered to recruit proactive inhibition as opposed to reactive inhibition. The animal can see the landmark as it approaches and can prepare to stop. The situation then lends itself to a potential locomotor plan that is implemented without being interrupted. The role of the hyperdirect pathway has been extensively studied in reactive settings (Aron et al., 2003; Eagle et al., 2008; Nachev et al., 2007, 2008). In stop-signal reaction tasks or go/no-go tasks, participants are signaled to immediately halt an ongoing (or to be initiated) action. Proactive inhibition is considered to be heavily mediated by the indirect pathway, but there is certainly evidence of the hyperdirect pathway, and more generally the same “stopping network,” as equally being involved (Aron, 2011; Meyer and Bucci, 2016). Our work also highlights a role for the hyperdirect pathway as a critical route for rapid cortical modulation of brainstem structures, complementing the classical role of the direct and indirect pathway and offering a view consistent with how the hyperdirect pathway is considered to interact with them (Schmidt et al., 2013). We believe that the hyperdirect pathway does indeed have a general role in interrupting action (Aron et al., 2016; Fife et al., 2017; Li et al., 2020). However, aspects of that role need not come through the pathway to MLR, but perhaps through pathways to the superior colliculus (SC) or thalamus through SNr. One can hypothesize that the role of the corticosubthalamic pathway toward SC may be in rapidly interrupting orienting behavior. The role of the hyperdirect pathway may well extend beyond motor processes, to associative and cognitive processes. Evidence of this generality is emerging (Heston et al., 2020; Hannah and Aron, 2021), and this role is still a subject of further research.

In addition to the indirect pathway in the basal ganglia, alternative routes for signaling locomotion halts may include a visual tectal pathway, consisting of direct projections from the SC to the MLRs (Roseberry et al., 2016). We expect such a signal to be more engaged upon sudden flashes of the landmark, likely in a more reactive setting, perhaps engaging circuits typically used for startle responses (Liang et al., 2015). In addition, glycinergic neurons in the pontine reticular formation (PRF) project to the intra-laminar thalamic nuclei (IL), and stimulation of their axons in IL produces behavioral arrest (Giber et al., 2015). M2 directly projects to PRF, and the projections may directly drive such glycinergic cells to achieve fast locomotion halts. Aside from these pathways, various other pathways can induce behavioral arrest (Klemm, 2001; Roseberry and Kreitzer, 2017). These are generally recruited via different mechanisms, although some can overlap with ours. Further task enhancements are needed to elucidate their contributions.

Limitations of the study

There are a number of limitations to the data and their interpretation that, if addressed, can further elucidate the underlying mechanisms. While calcium imaging provided us with projection-specific activity, the calcium signal dynamics are slow, and extracellular recordings while phototagging M2 cells projecting to STN may instead give us a temporally rich signal to better discern the dynamics of stopping. It is also unclear how strong the effects are of optogenetic activation or inhibition of axons on STN activity. Extracellular recordings during axonal stimulation may provide key information to understand the extent of the effect and its implications for behavior. We found that M2-STN inhibition yielded relatively weak behavioral effects, and such an experiment can help dissect the reasons. Finally, a main prediction of the work is that the STN-PPN and STN-SNr-PPN admit differential roles in ensuring rapid locomotion stops. Recording from STN projections to SNr and PPN through phototagging may elucidate the exact signatures sent along these two pathways.

STAR★METHODS

RESOURCE AVAILABILITY

Lead contact—Further information and requests for resources and reagents should be directed to and will be fulfilled by the Lead Contact, Elie Adam (eadam@mit.edu).

Materials availability—This study did not generate new unique reagents.

Data and code availability

- All data reported in this paper will be shared by the lead contact upon request.
- This paper does not report original code.
- Any additional information required to reanalyze the data reported in this paper is available from the lead contact upon request.

EXPERIMENTAL MODEL AND SUBJECT DETAILS

All procedures were approved by the Massachusetts Institute of Technology's Animal Care and Use Committee and conformed to the National Institutes of Health guidelines. Adult mice (>2 months old) on a C57BL/6J background were used in this study. Male or female mice were randomly selected for each experiment. We also used the Ai148D (Ai148(TIT2L-GC6f-ICL-tTA2)-D, Jackson Laboratory) mouse line for the two-photon imaging experiments, the VGlut2-Cre (VGlut2-ires-cre knock-in, Jackson Laboratory) mouse line for the optogenetics, optotagging experiments and tracing experiments and the vgat-Cre (VGlut2-ires-cre knock-in, Jackson Laboratory) mouse line for the optotagging experiments.

METHOD DETAILS

Surgery—Surgical procedures were performed under isoflurane anesthesia while maintaining body temperature at 37.5°C using an animal temperature controller (ATC2000, World Precision Instruments). After deep anesthesia was confirmed, mice were placed in a stereotaxic frame (51725D, Stoelting), scalp hairs were removed with hair-remover cream, the underlying skin was cleaned with 70% alcohol and betadine, and an incision was made in the scalp. The conjunctive tissue was removed by rubbing hydrogen peroxide on the skull. The skull was positioned such that the lambda and bregma marks were aligned on the anteroposterior and dorsoventral axes. The skull was further leveled along the mediolateral axis. Animals were given analgesia (slow release Buprenex, 0.1mg/kg and Meloxicam 0.1mg/kg) before and after surgery and their recovery was monitored daily for 72 h.

For viral injections, a 200-μm diameter hole was drilled through the skull at the location of interest. Viruses were delivered with a thin glass pipette at a rate of 75 nL/min (unless indicated otherwise) by an infuser system (QSI 53311, Stoelting). The following viruses (titer: ~10e-12 virus genomes per ml) were injected in the performed experiments: AAV5-CamKII-ChR2-mCherry (pAAV-CamKIIa-hChR2-(H134R)-mCherry-WPRE-pA, UNC Vector Core) for optogenetics activation of M2 axons in STN, AAVrg-EF1a-Cre-mCherry (pAAV-Ef1a-mCherry-IRES-Cre, Addgene) for 2P imaging of M2 neurons projecting to STN, AAV5-CaMKII-NpHR3.0 + EYFP (pAAV-CaMKIIa-eNpHR 3.0-EYFP, Addgene) for optogenetics inhibition of M2 axons in STN, AAVrg-CAG-Jaws + GFP-FLEX (pAAV-CAG-FLEX-rc [Jaws-KGC-GFP-ER2], Addgene) for optogenetics inhibition of STN somas projecting to PPN, AAV1-EF1a-ChR2+EYFP-DIO (AAV-EF1a-double floxed-hChR2(H134R)-EYFP-WPRE-HGHpA) for optotagging in PPN, AAV1-EF1a-ChR2+mCherry-DIO (pAAV-EF1a-double floxed-hChR2(H134R)-mCherry-WPRE-HGHpA) for optotagging in STN, AAVrg-EF1a-DO_DIO-tdTomato_EGFP (pAAV-Ef1a-DO_DIO-TdTomato_EGFP-WPRE-pA, Addgene) for anatomical tracing of STN projections to PPN, AAV5-CAG-GFP (pAAV-CAG-GFP, Addgene) for optogenetics control experiments.

For the optogenetic activation experiments, wild-type mice were unilaterally (left hemisphere) injected with 400nL of AAV5-CaMKII-ChR2-mCherry in M2 (centered at AP: +1mm, ML: +0.5mm, DV: +0.5mm). After injection, the skin was sutured and we let mice recover for 4–6 weeks for optimal opsin expression. In a second surgical procedure, a fiber-

optic cannula (Thorlabs) with 200um diameter (0.39NA) was implanted above STN (AP: −1.9mm, ML: +1.5mm, DV: +4.3mm). The optic fiber cannula was held by a stereotaxic manipulator, inserted and attached to the skull with dental cement (C&B Metabond, Parkell). To avoid light reflection and absorption, dental cement was mixed with black ink pigment (Black Iron Oxide 18727, Schmincke). A custom-designed headplate (eMachineShop) was implanted at the end of the surgery for head fixation. For the optogenetics experiment inhibiting the M2 axons in STN, wild-type mice were bilaterally injected with 400nL of AAV5-CaMKII-NpHR3.0-EYFP in M2, and a dual optic fiber cannula (Doric lens) was implanted with the two 200um diameter (0.39NA) fibers bilaterally lowered above STN (AP: −1.9mm, ML: +1.5mm, DV: +4.3mm). For the optogenetic experiment inhibiting the STN projections to PPN, VGlut2+ mice were bilaterally injected with 300nL of AAVrg-CAG-Jaws + GFP-FLEX in PPN (AP: −4.7mm, ML: +1.25mm, depth: +3.15mm from pial surface), and a dual optic fiber cannula (Doric lens) was implanted with the two 200um diameter (0.39NA) fibers bilaterally lowered above STN (AP: −1.9mm, ML: +1.5mm, DV: +4.3mm).

For the retrograde tracing of STN projections to PPN, VGlut2+ mice were bilaterally injected with 300nL of AAVrg-EF1a-DO_DIO-tdTomato_EGFP in PPN (AP: −4.7mm, ML: +1.25mm, depth: +3.15mm from pial surface). After injection, the skin was sutured and we let mice recover for 4 weeks for optimal opsin expression, before harvesting the brain for histology.

For imaging experiments, Ai148D mice were bilaterally injected with 200–300nL of AAVrg-EF1a-Cre-mCherry in STN (AP: −1.9mm, ML: +1.5mm, DV: +4.6mm) and a cranial window centered was implanted above M2 in both hemispheres. The virus was delivered at a slower rate of 50nL/min slowly to limit the spread as much as possible, to avoid contaminating adjascent brain regions. The location of STN also limits contamination: it is encapsulated by the cerebral peduncle from the anterior side, the ventral side, lateral side and half of the posterior side. We drilled a 3-mm circular window centered over the midline (AP: 1mm) to expose M2 on each hemisphere. We stacked two 3-mm coverslips centered on a 5-mm coverslip (CS-5R and CS-3R, Warner Instruments) and glued the three together with UV adhesive (NOA 61 UV adhesive, Norland Products). The fabricated window was positioned over the craniotomy and attached to the skull using dental cement (C&B Metabond, Parkell). The dental cement was mixed with black ink pigment (Black Iron Oxide 18727, Schmincke) to block light leakage during imaging. We then attached a custom-designed headplate to the skull for head fixation.

Extracellular single-unit recordings were performed acutely in head-fixed behaving mice. We attached a custom-designed headplate to the skull for head fixation, using a custom-designed stereotaxic arm to align the head plate parallel to the median and dorsal line of the skull during implantation. The head plate was attached to the skull using dental cement. The exposed skull was protected using rapid-curing silicone elastomer (Kwik-Cast, WPI) topped with a fine layer of dental cement. One to two days before recordings, mice were anesthetized with isoflurane and the dental cement and silicone elastomer on the skull were removed. The mouse was placed on the stereotaxic frame and 200-μm diameter craniotomies were performed on top of the recording sites of interest, M2 and PPN, centered

around the coordinates of interest. The craniotomy was protected with saline and a piece of Gelfoam (Pfizer). The skull was covered again with silicone and the animal was allowed to recover for at least a day. Viral injection were additionally performed before headplate attachment for optotagging experiments: 300nL of AAV1-EF1a-ChR2+EYFP-DIO were bilaterally injected in PPN of vlgut2-cre and vgat-cre mice (AP: −4.7mm, ML: +1.25mm, depth: +3.15mm from pial surface) for optotagging in PPN and 400nL of AAV1-EF1a-ChR2+EYFP-DIO were bilaterally injected in STN of VGlut2+ mice for optotagging in STN (AP: −1.9mm, ML: +1.5mm, DV: +4.7mm).

Behavioral task, equipment and training—Mice were head-fixed using optical hardware (Thorlabs) and positioned on a custom-fabricated rubber treadmill (LEGO Technic + M-D Building Products) coupled with a rotary encoder (Signswise). The virtual runway was constructed using two parallel rails (Thorlabs) each equipped with high-density LED PCB bars (DotStar, Adafruit). Reward consisted of 5–10ul of water and was delivered through a lick spout using a solenoid valve (Parker). Licks were collected, when needed, using a capacitive touch sensor (Adafruit). The behavioral apparatus was controlled through custom-written code deployed on a microcontroller (Arduino). The microcontroller interfaced, through serial connection, with custom-written scripts (Python) running on a custom-designed multi-purpose computer (operating under GNU/Linux) to execute the task.

The landmark consisted of a contiguous set of LEDs that were lit blue on both rails. The length of the landmark amounted to 6cm, and the position of the animal in track units (t.u.) was referenced to the mouse's nose. Specifically, the landmark interval 200–300 corresponded to the mouse's nose being within the lit LED range. Track units (t.u.) were calibrated to have 200t.u. correspond to 12cm. The rotation of the treadmill was coupled to the movement of the landmark so that the linear velocity of the outer-edge of the treadmill equaled the linear velocity of the landmark.

Mice underwent water-regulation and obtained water reward (5μL) during behavior. They were then habituated to the treadmill, and underwent a shaping procedure that rewards a stop after crossing a certain distance. The landmark was then introduced and the required waiting time to collect reward was gradually increased across days from 0.6s to 1.5s until they reached their full performance. Experiments began once the number of successful stops at the landmark was consistently above 100 within a 30 min session.

The behavioral experiment (Figure S1J) assessing the effect of landmark distance was performed by alternating between sessions having the landmark centered at position 250 (near) and sessions having the landmark centered at position 450 (far).

Behavioral model—From each behavioral session, we defined landmark-stop windows (rewarded stops between positions 200–300). Each time window corresponds to 2.5s, aligned to a switching point. The switching point was defined as the last major velocity peak (value higher than 25% of the maximum velocity within 200ms window before sustained zero velocity). The time window then consisted of 1s before the switching point, and 1.5s after. We chose this width to capture most of the 1.5s waiting period of the animal, and have the period where speed is decaying to a halt centered, thereby requiring the

switching point to be around 1s after the start of the window. Aligning to a switching point, instead of reward-time, allowed us to consider and analyze spontaneous stops that are non-rewarded. We pooled together all landmarks-stop windows, across sessions and animals, and averaged them to get the average traces, presented in (Figure 2C). We then fixed $u_{min} = 0$ to approximate the problem, and then derived τ and u_{max} from the peak velocity of the animal before stopping and the slope of the logarithm of the velocity trace during decay.

Optogenetic manipulations—Blue light (473nm) or amber light (589nm) was delivered using a diode-pumped solid-state laser (Optoengine for 473nm, Laserglow Technologies for 589nm). Laser stimulation was triggered using a custom-designed source-follower circuit driven by a microcontroller (Arduino) dictating the stimulation pattern. A fiber-optic patch cable with a ferrule end (200um, 0.39NA) was coupled to the implanted fiber optic cannula with a ferrule mating sleeve (Thorlabs). A piece of black electrical tape was wrapped around the connection between the patch cable and the implanted ferrule, to block any light emitted from that interface.

Photo-stimulation was randomly applied on 30% of the trials. We further imposed a condition that no two consecutive trials could be selected for laser stimulation. For the optogenetics activation experiments, on a trial selected for photo-stimulation, blue light was delivered once the animal reached position 100, for 500ms at 20Hz, 20% duty-cycle (PW:10ms, and T:50ms) with a peak power of 10–15mw (average power of 2–2.5mw). For the optogenetics inhibition experiments, on a trial selected for photo-stimulation, amber light was delivered once the animal reached position 175 continuously for either 1.5 s or till the animal crosses position 275, whichever time period is shorter. Each animal underwent three 30min behavioral sessions of photo-stimulation. We kept the session where the behavioral performance was deemed adequate (>50 hits).

Calcium imaging and neuronal response analysis—Two-photon calcium imaging was performed through a cranial window. GCaMP6f fluorescence was imaged through a 25x/1.05NA objective (Olympus) using a custom-configured two-photon microscope (MOM, Sutter Systems). Excitation light at 910nm was delivered with a Ti:Sapphire laser (Mai-Tai eHP, Spectra-Physics) equipped with dispersion compensation (DeepSee, Spectra-Physics). Emitted light was bandpass filtered and collected with a GaAsP photomultiplier tube (Hamamatsu). STN-projecting neurons in M2 were imaged between 400 and 500um below the surface at 10Hz using galvo scanning, and images were acquired by ScanImage (Vidrio) to generate a TIFF stack. Power at the objective ranged from 15 to 30 mW, depending on GCaMP6f expression level and depth.

Neuronal ROI selection and calcium signal extraction was performed using CaImAn (Flatiron Institute) (Giovannucci et al., 2019) implementing a constrained nonnegative matrix factorization approach (Pnevmatikakis et al., 2016). The obtained ROIs and signals were additionally hand-curated to leave out any false-positives.

The animals performed 30min behavioral sessions, and fluorescence was acquired for 1600s (~26.6 min) during that period. The behavioral data included a reference signal derived from the microscope acquisition trigger signal, and that signal was used to align to the

behavioral signals to the neural signals. The neural signals were then upsampled using piecewise-constant interpolation to match the temporal resolution of 200Hz of the behavior.

Data analysis: From each behavioral session we defined landmark-stop windows (rewarded, stops between positions 200–300) and spontaneous-stop windows (non-rewarded, stops before position 150). Each time window corresponds to 2.5s, aligned to a switching point. The switching point was defined as the last major velocity peak (above 25% of the maximum velocity within 200ms window before sustained zero velocity). The time window then consisted of 1s before the switching point, and 1.5s after.

For each neuron, we computed the average DFF response over a landmark-stop window, normalized each to a maximum DFF of 1, and formed an N-by-T (N: number of neurons and T: time) matrix M where each row corresponded to the normalized average DFF of a neuron. To capture most of the energy in the responses in a low-dimensional space, we reduced neuronal dimensions by performing a low-rank approximation (rank = 4). Specifically, we performed a singular value decomposition of M as $M = USV^T$ where the matrix S is a rectangular diagonal matrix of singular values, and the matrices U and V are orthonormal matrices (Dahleh et al., 2004; Horn and Johnson, 2012; Strang, 2016), and kept only the highest 4 singular values in S, and set the remaining ones to zero, to get a matrix S_{approx}. We reasoned that we had (not necessarily independent) four-degrees of freedom in our analysis: baseline, pre-stop, stop and post-stop activity, and thus sought to begin with a 4-dimensional space. Each of the four non-zero singular values in S corresponded to a temporal neuronal response in V^T, which together span a 4-dimensional subspace. The subspace contained more than 80% of the calcium signal energy for the whole population (squared Frobenius norm of M). Specifically, the sum of squares of all the entries (energy) in $M - M_{approx}$ is less than 20% of the sum of squares of all the entries (energy) in M, indicating that the low-dimensional subspace indeed captured 80% of the energy in the neuronal responses (Horn and Johnson, 2012; Strang, 2016). Adding more dimensions will only facilitate capturing more of the dynamics by capturing more energy. We aimed to capture the bulk features of the signal, avoiding less prominent features, more fit to be considered noise in these populations, by keeping the number of dimensions to a minimum.

The four temporal neuronal responses obtained in V^T corresponding to the non-zero singular values in S_{approx} span a 4-dimensional space, and form a basis to that space. Each DFF response can then be written as a weighted combination of these four basis responses and an additional response outside (orthogonal) to that space that is considered as noise. As a space can admit multiple bases, we decided to find a basis that represents stopping epochs and decompose our neuronal responses onto it. We sought to define ideal neuronal templates of pre-stop, stop and post-stop neurons (Figure S3A). We began with three signals equal to 1 for $t < 0$ while 0 otherwise, equal to the average velocity of the animal for $t > 0$ while 0 otherwise, and equal to 1 for $t > 0.5$s while 0 otherwise. We projected each of the three square signals to the 4-dimensional subspace defined by the low-rank approximation, and ensured orthogonality using the gram-schmidt orthonormalization process (Strang, 2016). We were left with three templates of ideal pre-stop, stop and post-stop neurons, spanning a three-dimensional subspace. We then kept the imaged neurons for which at least 85% of their calcium signal energy (area of the squared signal) came from the three-dimensional

subspace, and discarded the rest from the analysis. This kept about 64% of all neurons we started with, and we performed clustering on them as described below.

Each neuronal response can be written as a weighted combination of the three templates, plus some additional component orthogonal to the subspace (noise). We recovered the weights for each response by taking the inner-product (dot-product) with each template. We multiplied the weight by the maximum value in the template to account for the template width, to get a corrected weight. We then attributed a neuron to one of three classes (pre-stop, stop and post-stop) whose corresponding corrected-weight is highest.

Most importantly, the calcium responses in each class were not reduced in dimensions; they were the original averages of the raw DFF traces taken over landmark stop windows. The dimensionality reduction was only used to cluster the neuronal responses.

For the class of stop-neurons, we computed the weight with respect to the stop-neuron template for the average response in landmark-stop windows and spontaneous-stop windows, by taking the inner-product (dot-product) with the stop-neuron template.

For a fixed epoch and neuron, the activity of a trial was averaged over the epoch and normalized by the average over the whole stopping time window (between -1s and 1.5s, with 0 indicating the switching point). The reliability of a response was the computed as the coefficient of variation (mean/standard deviation). The epochs considered were: pre-stop (-1s–0s), stop (−0.25s–0.25s) and post-stop (0.5s–1.5s).

Extracellular recordings in M2 and PPN and neural response analysis—On the day of the recording, the animal was head-fixed on the behavioral setup and the silicone and Gelfoam removed gently. A 0.9% NaCl solution was used to keep the surface of the brain wet for the duration of the recordings. We submerged a reference silver wire in the NaCl solution on the skull surface. The 16-channel silicon probes (A1×16-Poly2-5mm-50s-177-A16, Neuronexus) were then lowered in the ventral axis with motorized manipulators (MP-285, Sutter Instrument Company and Micropositioner Model 660, Kopf) at a rate of 20 microns per second. The probe recording in M2 was lowered to (AP: +1mm, ML: +0.5mm, depth: +0.5mm from pial surface) and the probe recording in PPN was lowered to (AP: −4.7mm, ML: +1.25mm, depth: +3.15mm from pial surface). The recording sites on the probe span about 0.375mm. As such, the probe tip was lowered deeper than the indicated depth, to ensure the sites cover the area surrounding the indicated depth.

The extracellular signal was acquired through a custom-configured Plexon MAP system, initially amplified using a 1× gain head-stage (model E2a, Plexon) connected to a 100× preamp (PBX-247, Plexon). The signal was high-pass filtered at 300 Hz. Spikes were monitored online with amplitude threshold using Plexon Sort Client software, and raw continuous data was recorded at a rate of 40kHz. Spike sorting was then performed on the raw waveform using a fully-automated spike-sorting algorithm through Mountainsort (Chung et al., 2017). Spike curation was done manually to remove artifacts picked by the algorithms (ill-shaped spikes) and spikes with low amplitudes or low spontaneous spike rate (<0.1 spikes s^{-1}). We verified spike times with cross-correlograms to eliminate duplicates.

For verifying the probe location after recordings, the silicone probes were gently retracted and the recording tract was marked by re-entering the DiI-coated probe (2 mg/mL; D3911, ThermoFisher) at the same location. The brain was harvested post-experiment and the probe location was confirmed through histology.

Data analysis: The animals performed 30min behavioral sessions, and recordings were initiated before the start of a session and lasted after the end of a session. Both the behavioral and physiology apparatus were continuously recording an external reference signal (acquisition at 200Hz in behavioral data and 40kHz in physiology data). This signal was used to align the physiology and behavioral data.

We down-sampled the resolution of the physiology data by binning the spikes into 5ms intervals to match the resolution of the behavioral data, and computed mean average responses as performed for the calcium imaging. The data was smoothed with a Gaussian filter with standard deviation around 7ms (corresponding to a variance of $50ms^2$), and we then performed dimensionality reduction through low-rank approximation (with k = 4), exactly as performed for the calcium imaging data.

To study the relation between PPN activity and speed, we considered all the PPN neurons whose average activity transitions from high to low within a 1s window, 750ms before the switching point and 250ms after. Specifically, for each time point, we computed the mean h of the activity prior to it and the mean l of the activity after it, and found the time point that maximizes h-l. We kept the neurons whose optimal time point falls within the corresponding window. We went through all the kept neurons and all stops, paired the spiking activity of one neuron (binned into 5ms intervals to match the behavioral resolution) during a single stop with the position evolution corresponding to that stop window. We then averaged all the position traces, differentiated and smoothed the signal to obtain the speed trace. We similarly averaged all the spiking activity (corresponding to the different stop windows, pooling all the neurons together) and smoothed it to obtain the PPN trace. The smoothing is performed with a Gaussian convolution with standard deviation of about 7ms (var = $50ms^2$). We computed the standard error of the mean error values, similarly. We could then learn the variable a by computing the slope of the logarithm of the traces to get a rate of decay of 17.08, approximated thereafter by 17.

To reconstruct the M2 error, we first reconstructed its components, corresponding to the negative acceleration and the negative speed. To reconstruct the negative acceleration signal, we derived the negative acceleration from the speed, and projected it onto the low-dimensional subspace already derived from the neural responses to get the best neural approximation of it. This approximation is achieved by a weighted combination of neural responses where the weights can be either positive or negative. To ensure that the weights are non-negative, we recomputed a new set of weights on the average responses through non-negative least squares, so that a combination of the neural responses using the new non-negative weights matched the low-dimensional response. This yields a low-dimensional representation of the negative acceleration component with only non-negative weights. We repeated the procedure to derive a low-dimensional negative speed signal, beginning by projecting the negative of the speed signal onto the low dimensional space. Finally, the

error signal is a positive weighted combination of these two components. To recover these weights, we defined the theoretical impulse response function $ae^{-at}u(t)$. We then convolved the separate components with it to get their contribution to the PPN response. Using non-negative least squares, we found the optimal non-negative weights such that the weighted combination of the filtered components best fits the PPN response, leading to the predicted response. By linearity, these correspond to the weights in the original M2 error signal. We then repeated the whole process by removing the STN-PPN projection, and computed a new predicted response via an updated M2 error signal.

The reliability analysis is similar to that performed for the calcium imaging data.

Extracellular recordings in STN and neural response analysis—The preparation for the STN recordings followed the same procedure as that of M2 and PPN recordings. A motorized manipulator (Micropositioner Model 660, Kopf) was used to lower a Neuropixels 1.0 probe, at a rate of 20 microns per second, toward STN (AP: −1.9mm, ML: +1.5mm, DV: +4.5mm) to a depth of 5.5mm. The spikes analyzed were then restricted to be the ones found on channels corresponding to STN location, taken to be between 4.25mm and 5mm from the pial surface. The data was acquired using the standard Neuropixels hardware (IMEC) though SpikeGLX (HHMI/Janelia Research Campus). Spike sorting was performed using Kilosort2 (Pachitariu et al., 2016), and then hand-curated using Phy.

Probe location was also verified by using DiI after a recording session and harvesting the brain postexperiment to recover the probe track.

Data analysis: As in the M2 and PPN recordings, the animals performed 30min behavioral sessions, and recordings were initiated before the start of a session and lasted after the end of a session. Both the behavioral and physiology apparatus were simultaneously continuously recording an external reference signal (acquisition of 200Hz in behavioral data and 30kHz in physiology data). This signal was used to align the physiology and behavioral data.

The data was again down-sampled by binning the spikes into 5ms intervals to match the resolution of the behavioral data, and was processed as done for the M2 and PPN recordings.

To characterize the component of the dynamical state corresponding to the negative acceleration, we considered all the neurons whose average firing rate is its maximum in a 500ms interval, 250ms before the switching point and 250ms after. We performed a low-rank approximation (k = 5) and derived a low-dimensional subspace that explains most of the energy in the average responses. We computed the negative acceleration from the speed signal, and projected it onto this subspace to recover the neuronal signal representing it. We then took this neural signal, and convolved it with $h = e^{-at}u(t)$ to obtain its dynamical state counterpart. This convolution necessarily places the obtained signal outside the low-dimensional subspace, and we then projected it again onto the subspace to ensure that it belongs there. The neural signals representing the negative acceleration component and the dynamical counterpart are both obtained using a weighted combination of the average neural responses via positive and negative weights. To ensure the weights are non-negative, we recomputed a new set of weights (as done in the M2 and PPN data) on the

average responses through non-negative least squares, as a means to recover a signal using only non-negative weights that match the low-dimensional response of the non-negative acceleration component and its dynamical counterpart. These non-negative weights span a two-dimensional space, that explained a high amount of energy (39.63%) in the neuronal population response, as it is very close to being a subspace of the original 5-dimensional subspace. We repeated the same procedure to characterize the component of the dynamical state corresponding to the negative speed. For this, we considered all the STN neurons whose average activity transitioned from low to high starting within a 1s interval, 250ms before the switching point and 750ms after the switching point. This was performed using a procedure similar to that used to characterize PPN speed activity.

The reliability analysis is similar to that performed for the calcium imaging data.

Optotagging in PPN and STN—The preparation for the phototagging recordings followed the same procedure as that of the M2 and PPN recordings. A16-channel silicone optrode (A1×16-Poly2-5mm-50s-177-OA16LP, Neuronexus) was connected via a 105-μm/0.22 numerical aperture patch cable (M61L01, Thorlabs) to a solid-state blue laser (Opto Engine), and was lowered to the recording site of interest as done for PPN and STN. The tip of the optrode was first lowered to around 200um above the recording coordinates of interest, blue light was then periodically delivered (at a rate of 2Hz) while the optrode was then progessively lowered slowly in search for units responsive to light stimulation, adjusting the light stimulation intensity to reduce stimulation artifacts and observe neuronal responses. The final position of the probe was decided when units responsive to light stimulation were detected and the electrode recording sites spanned the recording area of interest.

At the beginning and end of each recording sessions, light pulses of 5 ms at a fixed light intensities (tuned between 0.1 and 1 mW for a given recording session as a function of evoked responses) were repeatedly delivered in the tissue (frequency: 2 Hz), to perform post-hoc comparison of spontaneous and light-evoked waveform for each sorted unit. Sorting and curation was performed as done for the M2 and PPN recordings. Units were considered light-responsive if they responded significantly using the SALT algorithm (Kvitsiani et al., 2013). We also only kept units responding within an 8-ms-period after light stimulus onset, and whose light-evoked waveforms closely matched the spontaneous ones. Analysis of neuronal responses was performed as done in the respective sections on PPN and STN recordings. The recording tract was also marked by coating the probe with DiI as performed for M2, PPN and STN recordings.

Histological methods and verification—Under very deep anesthesia, mice were perfused transcardially with 0.9% NaCl followed by 4%PFA. The brains were harvested and post-fixed in 4% PFA at 4°C overnight. In some experiments, brains were extracted without transcardial perfusion and only immersed in PFA overnight. Coronal or sagittal sections (100um thick) were cut using a vibratome (VT2008, Leica). Slices were mounted and imaged with a confocal system (TCS SP8, Leica) with 10x/0.40NA or 20X/0.75NA objectives (Leica).

Optogenetics: The position and depth of the fiber optic was assessed by delineating tissue damage along the fiber-optic track track following its removal during brain extraction. Placement was considered correct if the M2 axons in STN were found in proximity and within a narrow cone region to the optic fiber tip (0.39NA). Viral expression was considered adequate if cortical projection toward the subthalamic nucleus (through the cerebral peduncle) were strongly visible under the confocal microscope, and fluorescent axons were observed in STN. This applied to activation, inhibition and control experiments regarding the M2 projections to STN. For experiments silencing STN projections to PPN, viral expression was considered adequate if somas were observed in STN and the injection site corresponded to the PPN per the reference atlas. These verifications were performed using sagittal brain sections.

Imaging: The imaging location was determined by identify the center of window, obtained by adequate X- and Y-translations corresponding to the radius of the window starting from an edge, guided by the sinus in the middle of the window, and defining that center as an imaging reference. Imaging fields of view were determined and centered to be around 600um along the ML direction from the origin reference. All imaged neurons in the field of view were considered. This number was further reduced to those whose activity is 85% explained by the low dimensional activity space, as expounded in the section on data processing. Viral expression in M2 was assessed through the 2-photon microscope, and imaging was perfomed when expression showed a dynamic range in fluorescence due to calcium activity. Injection sites were inspected under the confocal microscope through sagittal brain sections, and considered adequated when targetted to the STN, observable under the confocal and additionally visually demarcated by structures observed under the confocal, such that the cerebral peduncle and the SNr.

M2 and PPN recordings: The probe recording in M2 was lowered to (AP: +1mm, ML: +0.5mm, depth: +0.5mm from pial surface) and the probe recording in PPN was lowered to (AP: −4.7mm, ML: +1.25mm, depth: +3.15mm from pial surface). The position of the probes was verified under the confocal microscope using DiI, and that of PPN was deemed correct by assessing proximity to the PAG and overlaying a referece atlas to demarcate PPN. These verifications were performed using coronal brain sections. The recording sites of the probe spanned 375um, and as such all sorted recorded units (with more than 500 spikes per session) were included at the start of the analysis. This number was further reduced to those whose activity is 85% explained by the low dimensional activity space, as expounded in the section on data processing.

STN recordings: All our neuropixels recordings in STN were performed with the same probe angle, starting from the same coordinates, going to the same depth of 5500um and thereby always reaching the same endpoint. These coordinates and angle were chosen during experimental design, using a reference atlas. This defined a fixed recording orientation and direction that crossed multiple brain region, then through the subthalamic nucleus and ended with the tip in the cerebral peduncle. As a check, we indeed observed changes along the probe length once channels were out of the cerebral peduncle, which corresponded to about 500um above the tip. We then recreated this direction on the reference brain atlas, recovered

the coordinates of recorded regions per the atlas including the STN, and mapped them to channels on the probe based on the geometry. All sorted recorded units (with more than 500 spikes per session) that we principally detected on recording sites corresponding the STN location were included in the analysis. The position of the probe was verified under the confocal microscope using DiI, and it was deemed correct if it corresponded to the same starting and endpoint considered by the reference atlas, determined by using brain structures visible under the confocal such as the cerebral peduncle, the STN and the hippocampus. These verifications were performed using sagittal brain sections.

Optotagging: In addition to the verifications performed for probe location during extracellular recordings, viral expression was assessed by assessing fluorescence in the recorded region. Verifications for PPN recordings were performed using coronal sections, and for STN recordings using sagittal sections.

QUANTIFICATION AND STATISTICAL ANALYSIS

The data was analyzed using Python 3, and the statistical test used along with the necessary statistical details are indicated in the corresponding figure legend. We utilized non-parametric whenever possible to avoid assumptions required for parametric tests.

Statistics for neuronal responses measurements and reliability relied on the Mann-Whitney U-test, unless specified otherwise. Statistics for all optogenetics bar plots were computed by pooling together all Laser OFF and Laser ON trials, and performing a permutation test with 20000 iterations. For the inhibition experiments, we additionally performed permutation tests by shuffling the trial labels for each animal separately and then pooling the data together, to account for within-subject dependencies (e.g., Aarts et al., 2014). This resulted in minor alterations to the p value obtained by directly pooling the data together, without changes to the significance.

Supplementary Material

Refer to Web version on PubMed Central for supplementary material.

ACKNOWLEDGMENTS

This work was supported by a JPB Foundation Fellowship (to E.M.A.), and NIH grants R01EY028219 and R01MH126351, the Picower Institute Innovation Fund, and the Simons Foundation Autism Research Initiative through the Simons Center for the Social Brain (to M.S.). We thank Dr. Vincent Breton-Provencher and Dr. Grayson Sipe for their careful reading of the manuscript, and members of the laboratory for their comments and advice.

REFERENCES

Aarts E, Verhage M, Veenvliet JV, Dolan CV, and Van Der Sluis S (2014). A solution to dependency: using multilevel analysis to accommodate nested data. Nat. Neurosci 17, 491–496. 10.1038/nn.3648. [PubMed: 24671065]

Alexander GE, DeLong MR, and Strick PL (1986). Parallel organization of functionally segregated circuits linking basal ganglia and cortex. Annu. Rev. Neurosci 9, 357–381. 10.1146/annurev.ne.09.030186.002041. [PubMed: 3085570]

Arber S, and Costa RM (2018). Connecting neuronal circuits for movement. Science 360, 1403–1404. 10.1126/science.aat5994. [PubMed: 29954969]

Aron AR (2011). From reactive to proactive and selective control: developing a richer model for stopping inappropriate responses. Biol. Psychiatry 69, e55–68. 10.1016/j.biopsych.2010.07.024. [PubMed: 20932513]

Aron AR, and Poldrack RA (2006). Cortical and subcortical contributions to stop signal response inhibition: role of the subthalamic nucleus. J. Neurosci 26, 2424–2433. 10.1523/JNEUROSCI.4682-05.2006. [PubMed: 16510720]

Aron AR, Fletcher PC, Bullmore ET, Sahakian BJ, and Robbins TW (2003). Stop-signal inhibition disrupted by damage to right inferior frontal gyrus in humans. Nat. Neurosci 6, 115–116. 10.1038/nn1003. [PubMed: 12536210]

Aron AR, Herz DM, Brown P, Forstmann BU, and Zaghloul K (2016). Frontosubthalamic circuits for control of action and cognition. J. Neurosci 36, 11489–11495. 10.1523/JNEUROSCI.2348-16.2016. [PubMed: 27911752]

Aström KJ, and Murray RM (2010). Feedback Systems: An Introduction for Scientists and Engineers (Princeton university press).

Attinger A, Wang B, and Keller GB (2017). Visuomotor coupling shapes the functional development of mouse visual cortex. Cell 169, 1291–1302.e14. 10.1016/j.cell.2017.05.023. [PubMed: 28602353]

Barthas F, and Kwan AC (2017). Secondary motor cortex: where 'sensory' Meets 'motor' in the rodent frontal cortex. Trends Neurosci. 40, 181–193. 10.1016/j.tins.2016.11.006. [PubMed: 28012708]

Baunez C, and Robbins TW (1997). Bilateral lesions of the subthalamic nucleus induce multiple deficits in an attentional task in rats. Eur. J. Neurosci 9, 2086–2099. 10.1111/j.1460-9568.1997.tb01376.x. [PubMed: 9421169]

Bertsekas DP (1995). Dynamic Programming and Optimal Control (Athena scientific Belmont).

Bolam JP, Hanley JJ, Booth PC, and Bevan MD (2000). Synaptic organisation of the basal ganglia. J. Anat 196, 527–542. 10.1046/j.1469-7580.2000.19640527.x. [PubMed: 10923985]

Bouvier J, Caggiano V, Leiras R, Caldeira V, Bellardita C, Balueva K, Fuchs A, and Kiehn O (2015). Descending command neurons in the brainstem that halt locomotion. Cell 163, 1191–1203. 10.1016/j.cell.2015.10.074. [PubMed: 26590422]

Caggiano V, Leiras R, Goñi-Erro H, Masini D, Bellardita C, Bouvier J, Caldeira V, Fisone G, and Kiehn O (2018). Midbrain circuits that set locomotor speed and gait selection. Nature 553, 455–460. 10.1038/nature25448. [PubMed: 29342142]

Capelli P, Pivetta C, Soledad Esposito M, and Arber S (2017). Locomotor speed control circuits in the caudal brainstem. Nature 551, 373–377. 10.1038/nature24064. [PubMed: 29059682]

Chen W, de Hemptinne C, Miller AM, Leibbrand M, Little SJ, Lim DA, Larson PS, and Starr PA (2020). Prefrontal-subthalamic hyperdirect pathway modulates movement inhibition in humans. Neuron 106, 579–588.e3. 10.1016/j.neuron.2020.02.012. [PubMed: 32155442]

Chung JE, Magland JF, Barnett AH, Tolosa VM, Tooker AC, Lee KY, Shah KG, Felix SH, Frank LM, and Greengard LF (2017). A fully automated approach to spike sorting. Neuron 95, 1381–1394.e6. 10.1016/j.neuron.2017.08.030. [PubMed: 28910621]

Chuong AS, Miri ML, Busskamp V, Matthews GA, Acker LC, Sørensen AT, Young A, Klapoetke NC, Henninger MA, Kodandaramaiah SB, et al. (2014). Noninvasive optical inhibition with a red-shifted microbial rhodopsin. Nat. Neurosci 17 (8), 1123–1129. [PubMed: 24997763]

Churchland MM, Cunningham JP, Kaufman MT, Ryu SI, and Shenoy KV (2010). Cortical preparatory activity: representation of movement or first cog in a dynamical Machine? Neuron 68, 387–400. 10.1016/j.neuron.2010.09.015. [PubMed: 21040842]

Dahleh M, Dahleh MA, and Verghese G (2004). Lectures on Dynamic Systems and Control.

Drew T, Prentice S, and Schepens B (2004). Cortical and brainstem control of locomotion. Prog. Brain Res 143, 251–261. 10.1016/S0079-6123(03)43025-2. [PubMed: 14653170]

Eagle DM, Baunez C, Hutcheson DM, Lehmann O, Shah AP, and Robbins TW (2008). Stop-signal reaction-time task performance: role of prefrontal cortex and subthalamic nucleus. Cereb. Cortex 18, 178–188. 10.1093/cercor/bhm044. [PubMed: 17517682]

Economo MN, Viswanathan S, Tasic B, Bas E, Winnubst J, Menon V, Graybuck LT, Nguyen TN, Smith KA, Yao Z, et al. (2018). Distinct descending motor cortex pathways and their roles in movement. Nature 563, 79–84. 10.1038/s41586-018-0642-9. [PubMed: 30382200]

Esposito MS, and Arber S (2016). Motor control: illuminating an enigmatic midbrain locomotor center. Curr. Biol 26, R291–R293. 10.1016/j.cub.2016.02.043. [PubMed: 27046818]

Ferreira-Pinto MJ, Ruder L, Capelli P, and Arber S (2018). Connecting circuits for supraspinal control of locomotion. Neuron 100, 361–374. 10.1016/j.neuron.2018.09.015. [PubMed: 30359602]

Fife KH, Gutierrez-Reed NA, Zell V, Bailly J, Lewis CM, Aron AR, and Hnasko TS (2017). Causal role for the subthalamic nucleus in interrupting behavior. Elife 6, e27689. 10.7554/eLife.27689. [PubMed: 28742497]

Freeze BS, Kravitz AV, Hammack N, Berke JD, and Kreitzer AC (2013). Control of basal ganglia output by direct and indirect pathway projection neurons. J. Neurosci 33, 18531–18539. 10.1523/JNEUR-OSCI.1278-13.2013. [PubMed: 24259575]

Giber K, Diana MA, M Plattner V, Dugué GP, Bokor H, Rousseau CV, Maglóczky Z, Havas L, Hangya B, Wildner H, et al. (2015). A subcortical inhibitory signal for behavioral arrest in the thalamus. Nat. Neurosci 18, 562–568. 10.1038/nn.3951. [PubMed: 25706472]

Giovannucci A, Friedrich J, Gunn P, Kalfon J, Brown BL, Koay SA, Taxidis J, Najafi F, Gauthier JL, Zhou P, et al. (2019). CaImAn an open source tool for scalable calcium imaging data analysis. Elife 8, e38173. 10.7554/eLife.38173. [PubMed: 30652683]

Goulding M (2009). Circuits controlling vertebrate locomotion: moving in a new direction. Nat. Rev. Neurosci 10, 507–518. 10.1038/nrn2608. [PubMed: 19543221]

Grätsch S, Auclair F, Demers O, Auguste E, Hanna A, Büschges A, and Dubuc R (2019). A brainstem neural substrate for stopping locomotion. J. Neurosci 39, 1044–1057. 10.1523/JNEUROSCI.1992-18.2018. [PubMed: 30541913]

Graybiel AM (2000). The basal ganglia. Curr. Biol 10, R509–R511. 10.1016/S0960-9822(00)00593-5. [PubMed: 10899013]

Grillner S (2003). The motor infrastructure: from ion channels to neuronal networks. Nat. Rev. Neurosci 4, 573–586. 10.1038/nrn1137. [PubMed: 12838332]

Grillner S, Wallén P, Saitoh K, Kozlov A, and Robertson B (2008). Neural bases of goal-directed locomotion in vertebrates—an overview. Brain Res. Rev 57, 2–12. 10.1016/j.brainresrev.2007.06.027. [PubMed: 17916382]

Guillaumin A, Serra GP, Georges F, and Wallén-Mackenzie Å (2021). Experimental investigation into the role of the subthalamic nucleus (STN) in motor control using optogenetics in mice. Brain Res. 1755, 147226. 10.1016/j.brainres.2020.147226. [PubMed: 33358727]

Hamani C, Saint-Cyr JA, Fraser J, Kaplitt M, and Lozano AM (2004). The subthalamic nucleus in the context of movement disorders. Brain 127, 4–20. 10.1093/brain/awh029. [PubMed: 14607789]

Hannah R, and Aron AR (2021). Towards real-world generalizability of a circuit for action- stopping. Nat. Rev. Neurosci 22, 538–552. 10.1038/s41583-021-00485-1. [PubMed: 34326532]

Heindorf M, Arber S, and Keller GB (2018). Mouse motor cortex coordinates the behavioral response to unpredicted sensory feedback. Neuron 99, 1040–1054.e5. 10.1016/j.neuron.2018.07.046. [PubMed: 30146302]

Heston J, Friedman A, Baqai M, Bavafa N, Aron AR, and Hnasko TS (2020). Activation of subthalamic nucleus stop circuit disrupts cognitive performance. eNeuro 7, ENEURO.0159–20.2020. 10.1523/eneuro.0159-20.2020.

Hintiryan H, Foster NN, Bowman I, Bay M, Song MY, Gou L, Yamashita S, Bienkowski MS, Zingg B, Zhu M, et al. (2016). The mouse cortico-striatal projectome. Nat. Neurosci 19, 1100–1114. 10.1038/nn.4332. [PubMed: 27322419]

Hooks BM, Papale AE, Paletzki RF, Feroze MW, Eastwood BS, Couey JJ, Winnubst J, Chandrashekar J, and Gerfen CR (2018). Topographic precision in sensory and motor corticostriatal projections varies across cell type and cortical area. Nat. Commun 9, 3549. 10.1038/s41467-018-05780-7. [PubMed: 30177709]

Horn RA, and Johnson CR (2012). Matrix Analysis, 2nd ed. (Cambridge University Press).

Huang J, Isidori A, Marconi L, Mischiati M, Sontag E, and Wonham WM (2018). Internal models in control, biology and neuroscience. In 2018 IEEE Conference on Decision and Control (CDC).

Presented at the 2018 IEEE Conference on Decision and Control (CDC), pp. 5370–5390. 10.1109/CDC.2018.8619624.

Josset N, Roussel M, Lemieux M, Lafrance-Zoubga D, Rastqar A, and Bretzner F (2018). Distinct contributions of mesencephalic locomotor region nuclei to locomotor control in the freely behaving mouse. Curr. Biol 28, 884–901.e3. 10.1016/j.cub.2018.02.007. [PubMed: 29526593]

Juvin L, Grätsch S, Trillaud-Doppia E, Gariépy J-F, Büschges A, and Dubuc R (2016). A specific population of reticulospinal neurons controls the termination of locomotion. Cell Rep. 15, 2377–2386. 10.1016/j.celrep.2016.05.029. [PubMed: 27264174]

Keller GB, and Mrsic-Flogel TD (2018). Predictive processing: a canonical cortical computation. Neuron 100, 424–435. 10.1016/j.neuron.2018.10.003. [PubMed: 30359606]

Kiehn O (2006). Locomotor circuits in the mammalian spinal cord. Annu. Rev. Neurosci 29, 279–306. 10.1146/annurev.neuro.29.051605.112910. [PubMed: 16776587]

Kiehn O (2016). Decoding the organization of spinal circuits that control locomotion. Nat. Rev. Neurosci 17, 224–238. 10.1038/nrn.2016.9. [PubMed: 26935168]

Kim LH, Sharma S, Sharples SA, Mayr KA, Kwok CHT, and Whelan PJ (2017). Integration of descending command systems for the generation of context-specific locomotor behaviors. Front. Neurosci 11. 10.3389/fnins.2017.00581.

Klemm WR (2001). Behavioral arrest: in search of the neural control system. Prog. Neurobiol 65, 453–471. 10.1016/S0301-0082(01)00016-8. [PubMed: 11689281]

Kvitsiani D, Ranade S, Hangya B, Taniguchi H, Huang JZ, and Kepecs A (2013). Distinct behavioural and network correlates of two interneuron types in prefrontal cortex. Nature 498, 363–366. 10.1038/nature12176. [PubMed: 23708967]

Li B, Nguyen TP, Ma C, and Dan Y (2020). Inhibition of impulsive action by projection-defined prefrontal pyramidal neurons. Proc. Natl. Acad. Sci. USA 117, 17278–17287. 10.1073/pnas.2000523117. [PubMed: 32631999]

Liang F, Xiong XR, Zingg B, Ji XY, Ji X, Zhang LI, and Tao HW (2015). Sensory cortical control of a visually induced arrest behavior via corticotectal projections. Neuron 86, 755–767. 10.1016/j.neuron.2015.03.048. [PubMed: 25913860]

Liu D, Ma C, Zheng W, Yao Y, and Dan Y (2018). Sleep and motor control by a basal ganglia circuit. Preprint at bioRxiv. 10.1101/405324.

Mandelbaum G, Taranda J, Haynes TM, Hochbaum DR, Huang KW, Hyun M, Umadevi Venkataraju K, Straub C, Wang W, Robertson K, et al. (2019). Distinct cortical-thalamic-striatal circuits through the parafascicular nucleus. Neuron 102, 636–652.e7. 10.1016/j.neuron.2019.02.035. [PubMed: 30905392]

Marple-Horvat DE, Amos AJ, Armstrong DM, and Criado JM (1993). Changes in the discharge patterns of cat motor cortex neurones during unexpected perturbations of on-going locomotion. J. Physiol 462, 87–113. 10.1113/jphysiol.1993.sp019545. [PubMed: 8331599]

McNamee D, and Wolpert DM (2019). Internal models in biological control. Annu. Rev. Control Robot. Auton. Syst 2, 339–364. 10.1146/annurev-control-060117-105206. [PubMed: 31106294]

Meyer HC, and Bucci DJ (2016). Neural and behavioral mechanisms of proactive and reactive inhibition. Learn. Mem 23, 504–514. 10.1101/lm.040501.115. [PubMed: 27634142]

Nachev P, Wydell H, O'Neill K, Husain M, and Kennard C (2007). The role of the pre-supplementary motor area in the control of action. Neuroimage 36, T155–T163. 10.1016/j.neuroimage.2007.03.034. [PubMed: 17499162]

Nachev P, Kennard C, and Husain M (2008). Functional role of the supplementary and pre-supplementary motor areas. Nat. Rev. Neurosci 9, 856–869. 10.1038/nrn2478. [PubMed: 18843271]

Nambu A, Tokuno H, Hamada I, Kita H, Imanishi M, Akazawa T, Ikeuchi Y, and Hasegawa N (2000). Excitatory cortical inputs to pallidal neurons via the subthalamic nucleus in the Monkey. J. Neurophysiol 84, 289–300. 10.1152/jn.2000.84.1.289. [PubMed: 10899204]

Nambu A, Tokuno H, and Takada M (2002). Functional significance of the cortico–subthalamo–pallidal 'hyperdirect' pathway. Neurosci. Res 43, 111–117. 10.1016/S0168-0102(02)00027-5. [PubMed: 12067746]

Oppenheim AV, Willsky AS, and Nawab SH (1996). Signals & Systems, Second edition (Prentice-Hall, Inc.).

Pachitariu M, Steinmetz N, Kadir S, Carandini M, and Kenneth DH (2016). Kilosort: realtime spike-sorting for extracellular electrophysiology with hundreds of channels. Preprint at bioRxiv. 10.1101/061481.

Parolari L, Schneeberger M, Heintz N, and Friedman JM (2021). Functional analysis of distinct populations of subthalamic nucleus neurons on Parkinson's disease and OCD-like behaviors in mice. Mol. Psychiatry 26, 7029–7046. 10.1038/s41380-021-01162-6. [PubMed: 34099874]

Pnevmatikakis EA, Soudry D, Gao Y, Machado TA, Merel J, Pfau D, Reardon T, Mu Y, Lacefield C, Yang W, et al. (2016). Simultaneous denoising, deconvolution, and demixing of calcium imaging data. Neuron 89, 285–299. 10.1016/j.neuron.2015.11.037. [PubMed: 26774160]

Roseberry T, and Kreitzer A (2017). Neural circuitry for behavioural arrest. Philos. Trans. R. Soc. Lond. B Biol. Sci 372, 20160197. 10.1098/rstb.2016.0197. [PubMed: 28242731]

Roseberry TK, Lee AM, Lalive AL, Wilbrecht L, Bonci A, and Kreitzer AC (2016). Cell-type-specific control of brainstem locomotor circuits by basal ganglia. Cell 164, 526–537. 10.1016/j.cell.2015.12.037. [PubMed: 26824660]

Ryczko D, and Dubuc R (2013). The multifunctional mesencephalic locomotor region. Curr. Pharm. Des 19, 4448–4470. 10.2174/1381612811319240011. [PubMed: 23360276]

Saunders A, Johnson CA, and Sabatini BL (2012). Novel recombinant adeno-associated viruses for Cre activated and inactivated transgene expression in neurons. Front. Neural Circuits 6, 47. 10.3389/fncir.2012.00047. [PubMed: 22866029]

Schmidt R, Leventhal DK, Mallet N, Chen F, and Berke JD (2013). Canceling actions involves a race between basal ganglia pathways. Nat. Neurosci 16, 1118–1124. 10.1038/nn.3456. [PubMed: 23852117]

Schultz W (1998). Predictive reward signal of dopamine neurons. J. Neurophysiol 80, 1–27. 10.1152/jn.1998.80.1.1. [PubMed: 9658025]

Schweizer N, Pupe S, Arvidsson E, Nordenankar K, Smith-Anttila CJA, Mahmoudi S, Andrén A, Dumas S, Rajagopalan A, Lévesque D, et al. (2014). Limiting glutamate transmission in a Vglut2-expressing subpopulation of the subthalamic nucleus is sufficient to cause hyperlocomotion. Proc. Natl. Acad. Sci. USA 111, 7837–7842. 10.1073/pnas.1323499111. [PubMed: 24821804]

Shenoy KV, Sahani M, and Churchland MM (2013). Cortical control of arm movements: a dynamical systems perspective. Annu. Rev. Neurosci 36, 337–359. 10.1146/annurev-neuro-062111-150509. [PubMed: 23725001]

Shik ML, Severin FV, and Orlovsky GN (1969). Control of walking and running by means of electrical stimulation of the mesencephalon. Electroencephalogr. Clin. Neurophysiol 26, 549.

Strang G (2016). Introduction to Linear Algebra, 6th edition (Wellesley-Cambridge Press).

Svoboda K, and Li N (2018). Neural mechanisms of movement planning: motor cortex and beyond. Curr. Opin. Neurobiol 49, 33–41. 10.1016/j.conb.2017.10.023. [PubMed: 29172091]

Swann NC, Cai W, Conner CR, Pieters TA, Claffey MP, George JS, Aron AR, and Tandon N (2012). Roles for the pre-supplementary motor area and the right inferior frontal gyrus in stopping action: electrophysiological responses and functional and structural connectivity. Neuroimage 59, 2860–2870. 10.1016/j.neuroimage.2011.09.049. [PubMed: 21979383]

Todorov E (2004). Optimality principles in sensorimotor control. Nat. Neurosci 7, 907–915. 10.1038/nn1309. [PubMed: 15332089]

Todorov E, and Jordan MI (2002). Optimal feedback control as a theory of motor coordination. Nat. Neurosci 5, 1226–1235. 10.1038/nn963. [PubMed: 12404008]

Uslaner JM, and Robinson TE (2006). Subthalamic nucleus lesions increase impulsive action and decrease impulsive choice mediation by enhanced incentive motivation? Eur. J. Neurosci 24, 2345–2354. 10.1111/j.1460-9568.2006.05117.x. [PubMed: 17074055]

Wessel JR, and Aron AR (2017). On the globality of motor suppression: unexpected events and their influence on behavior and cognition. Neuron 93, 259–280. 10.1016/j.neuron.2016.12.013. [PubMed: 28103476]

Whelan PJ (1996). Control of locomotion in the decerebrate cat. Prog. Neurobiol 49, 481–515. 10.1016/0301-0082(96)00028-7. [PubMed: 8895997]

Wolpert DM, and Ghahramani Z (2000). Computational principles of movement neuroscience. Nat. Neurosci 3, 1212–1217. 10.1038/81497. [PubMed: 11127840]

Wong AL, Haith AM, and Krakauer JW (2015). Motor planning. Neuroscientist 21, 385–398. 10.1177/1073858414541484. [PubMed: 24981338]

Yamawaki N, Radulovic J, and Shepherd GMG (2016). A corticocortical circuit directly links retrosplenial cortex to M2 in the mouse. J. Neurosci 36, 9365–9374. 10.1523/JNEUROSCI.1099-16.2016. [PubMed: 27605612]

Zhang S, Xu M, Kamigaki T, Hoang Do JP, Chang W-C, Jenvay S, Miyamichi K, Luo L, and Dan Y (2014). Long-range and local circuits for top-down modulation of visual cortex processing. Science 345, 660–665. 10.1126/science.1254126. [PubMed: 25104383]

Zhang S, Xu M, Chang W-C, Ma C, Hoang Do JP, Jeong D, Lei T, Fan JL, and Dan Y (2016). Organization of long-range inputs and outputs of frontal cortex for top-down control. Nat. Neurosci 19, 1733–1742. 10.1038/nn.4417. [PubMed: 27749828]

Highlights

- We developed a visually guided locomotion task to study stop signaling
- M2-STN projection sends a stop signal on visually guided locomotion stops
- M2-STN activity bidirectionally controls visually guided locomotion stops
- M2-STN pathways to MLR/PPN carry out differentiation for rapid locomotion control

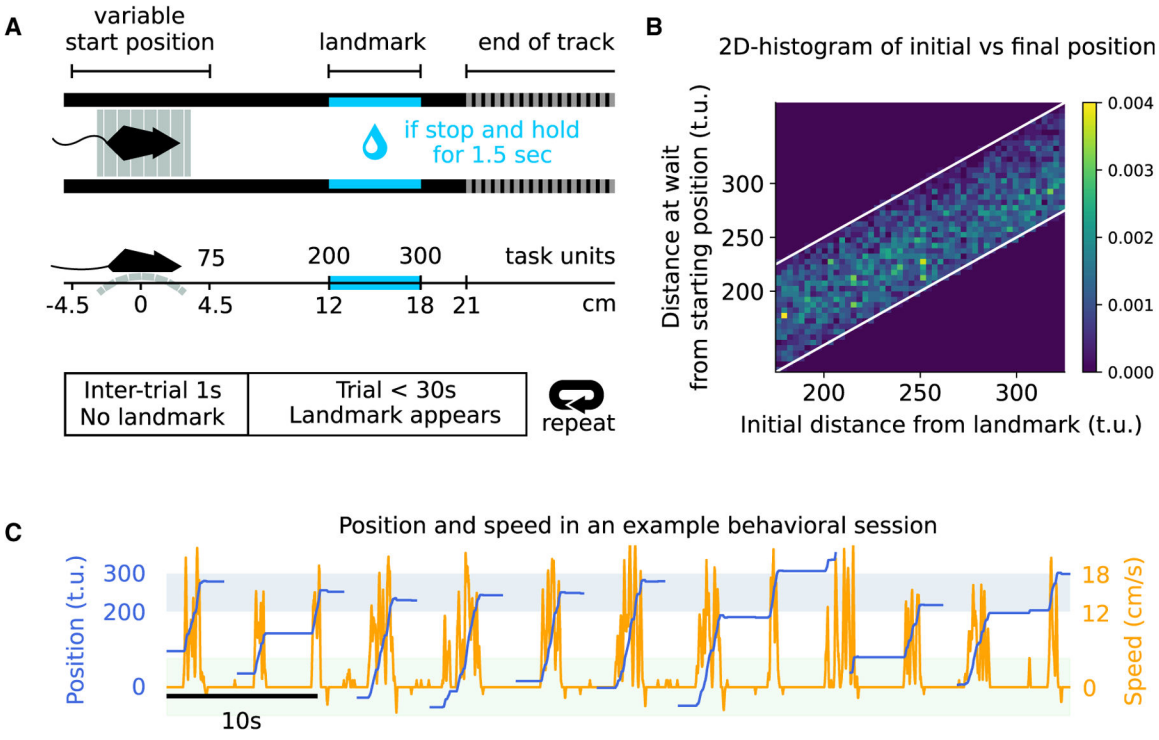

Figure 1. Mice were trained to run, stop, and wait at visual landmarks to collect reward

(A) Schematic showing the task design. Position is defined in terms of track units (t.u.), with 200 t.u. corresponding to 12 cm.

(B) Graph showing the distance at wait from starting position versus the distance from the landmark at the beginning of each trial. The color gradient indicates the frequency of stopping at the corresponding distance. The white lines indicate the beginning and end of the landmark. The distance of the landmark from the initial position does not affect the final stop position of the animal, indicating that the animals are using the visual cues, instead of relying on other mechanisms. N = 10 mice, 3 sessions each, between 100 and 250 hit trials each.

(C) Example data showing the position of a mouse on the track and its underlying speed for 9 trials. The blue- and green-shaded area indicates landmark position and potential starting position, respectively.

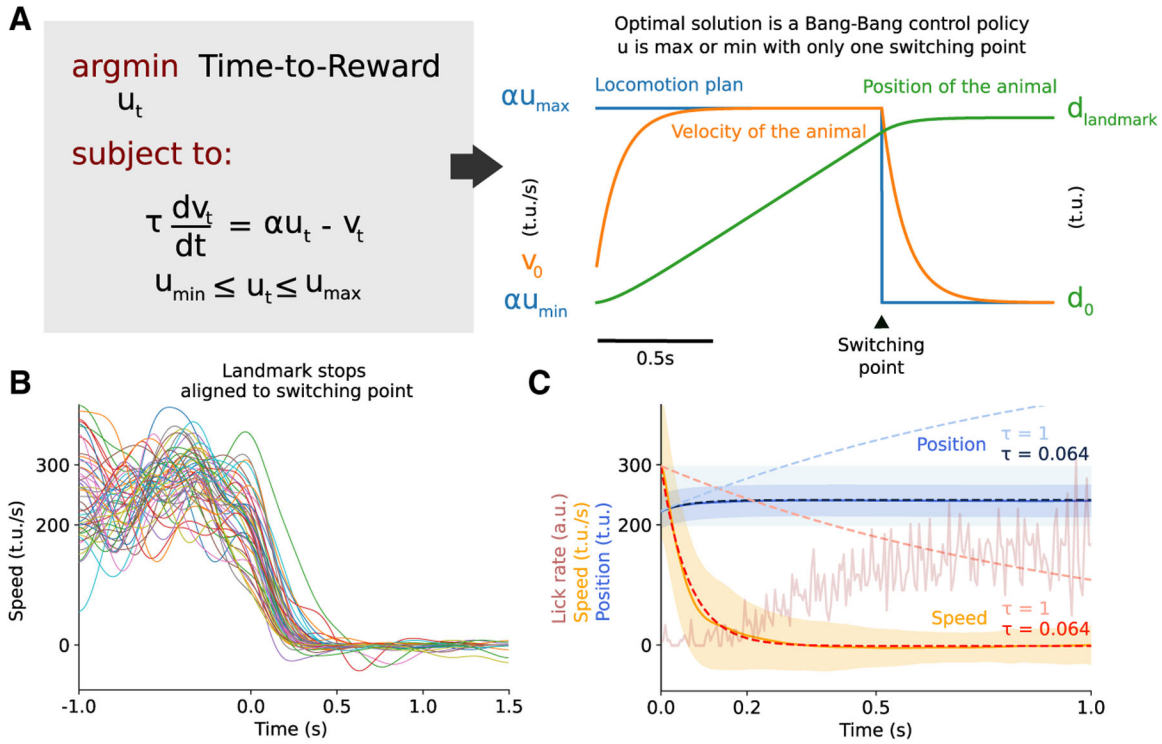

Figure 2. The behavior suggests a sudden switch in locomotion state

(A) Left: Formulation of the behavior as a minimumtime optimal-control problem. The mouse is tasked to select a locomotor plan (u_t) that minimizes the time required to collect reward. The locomotor plan dictates the speed of the animal, and the relation is governed by a first-order ordinary differential equation, parametrized by a time constant **τ**. Furthermore, the locomotor plan, and therefore the speed, are bounded and cannot be infinite. Right: The optimal solution is a bang-bang control policy, where u_t starts at its maximum and suddenly switches to its minimum.

(B) Examples of speed traces in landmark-stop windows aligned to the last peak in velocity before stopping, indicating the “switching point” (30 trials drawn from all of the sessions across animals. N = 10 mice, 3 sessions each).

(C) Graph of the average speed, position, lick rate, and model fits (dashed line) to actual data (continuous line) for speed and position in the period immediately following the switching point (N = 10 mice, 3 sessions each). Modeled position and speed using the equation in (A) identified a time constant **τ** = 63.75 ms are depicted with dark blue and red dashed lines. Predicted position and speed with **τ** = 1 s are depicted with light blue and light red dashed lines. The shaded regions correspond to the standard deviation of the sampled distribution. N = 10 mice, 3 sessions each.

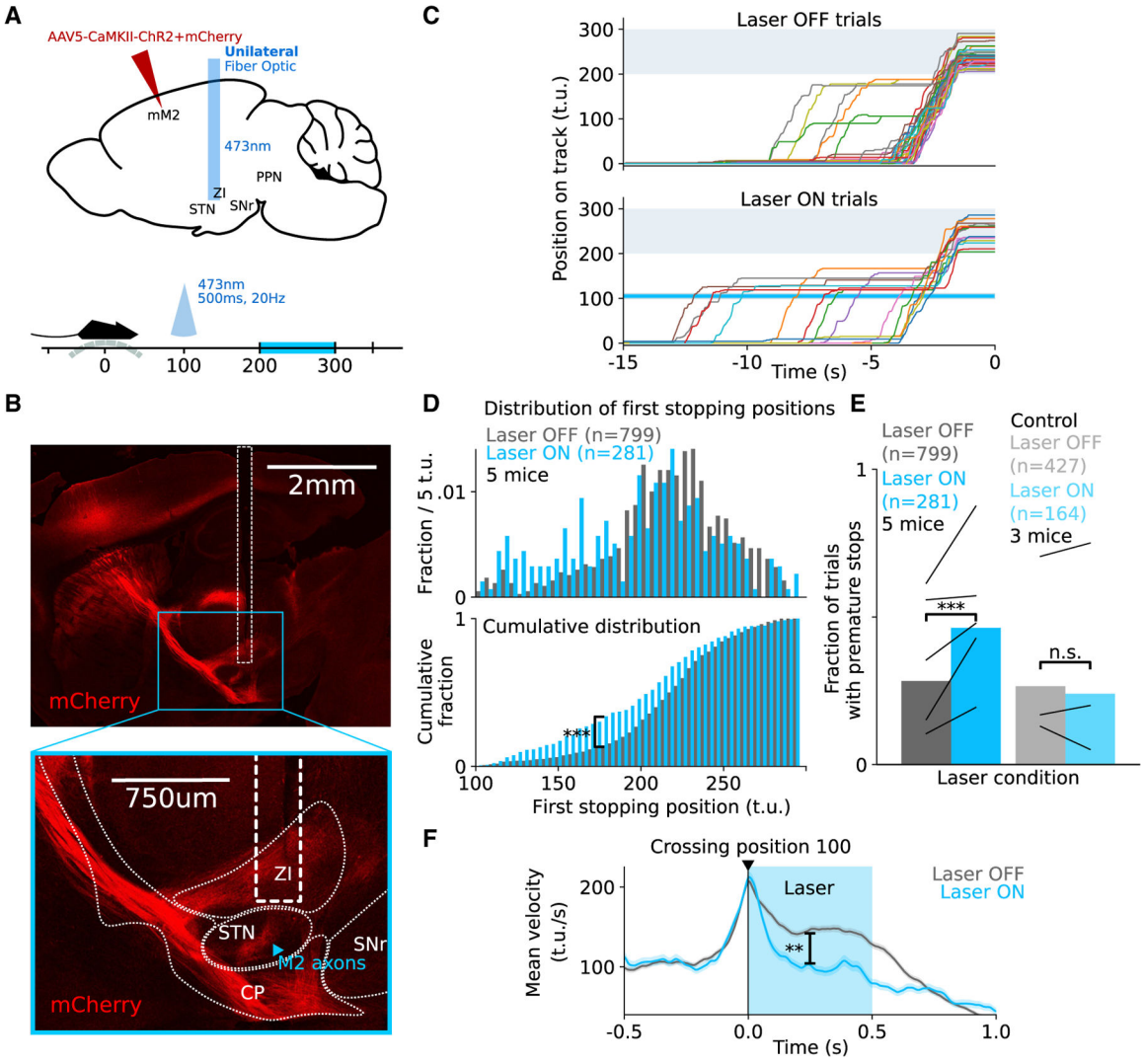

Figure 3. Activating M2 axons in STN leads to stopping

(A) An AAV virus expressing ChR2 was unilaterally injected in M2 of wild-type mice (N = 5 mice) and an optic fiber implanted over STN (ipsilateral to the injection site) to optogenetically target M2 axons in STN. On pseudorandom trials, blue light (473nm) was presented for 500 ms at 20 Hz as soon as the animal crossed track position 100.

(B) M2 projects directly to STN via the hyperdirect pathway. The image shows the projections (mCherry) and a fiber-optic placement.

(C) Position traces showing laser on and off hit trials aligned to reward time for 1 session in 1 animal. The blue line indicates the position at which the laser is turned on. To ensure enough running distance to position 100 and have it be a midpoint, the optogenetics sessions were performed at a fixed starting position of 0, although mice were trained on variable landmark distance.

(D) Plots showing the distribution of the first position the animal stops at after position 100 (N = 5 mice). We observe a shift in the distribution, toward position 100, indicating that during laser on trials, the animal stopped prematurely (Kolmogorov-Smirnov test, ***p = 4.76e−8 < 0.005).

(E) Plot showing the fraction of hits trials with premature stops (stopping first before position 200) (N = 5 mice) during laser on and off trials (permutation test, ***p = 0.0 < 0.005) and for control experiments (N = 3 mice) expressing GFP instead of ChR2 during laser on and off trials.

(F) Plot showing the average speed of the animal (N = 5 mice) in laser on and off trials aligned to the time of crossing position 100, with a significant difference between laser on and off trials after crossing position 100 (Mann-Whitney *U* test, **p = 0.0034). The blue-shaded area shows the period in which the laser is delivered. The peak of velocity at position 100 is an effect from averaging; as speed fluctuates, it is high while the animal is crossing position 100. Averaging will then yield a high average speed at position 100, and lower average elsewhere where peaks and troughs in speed are averaged.

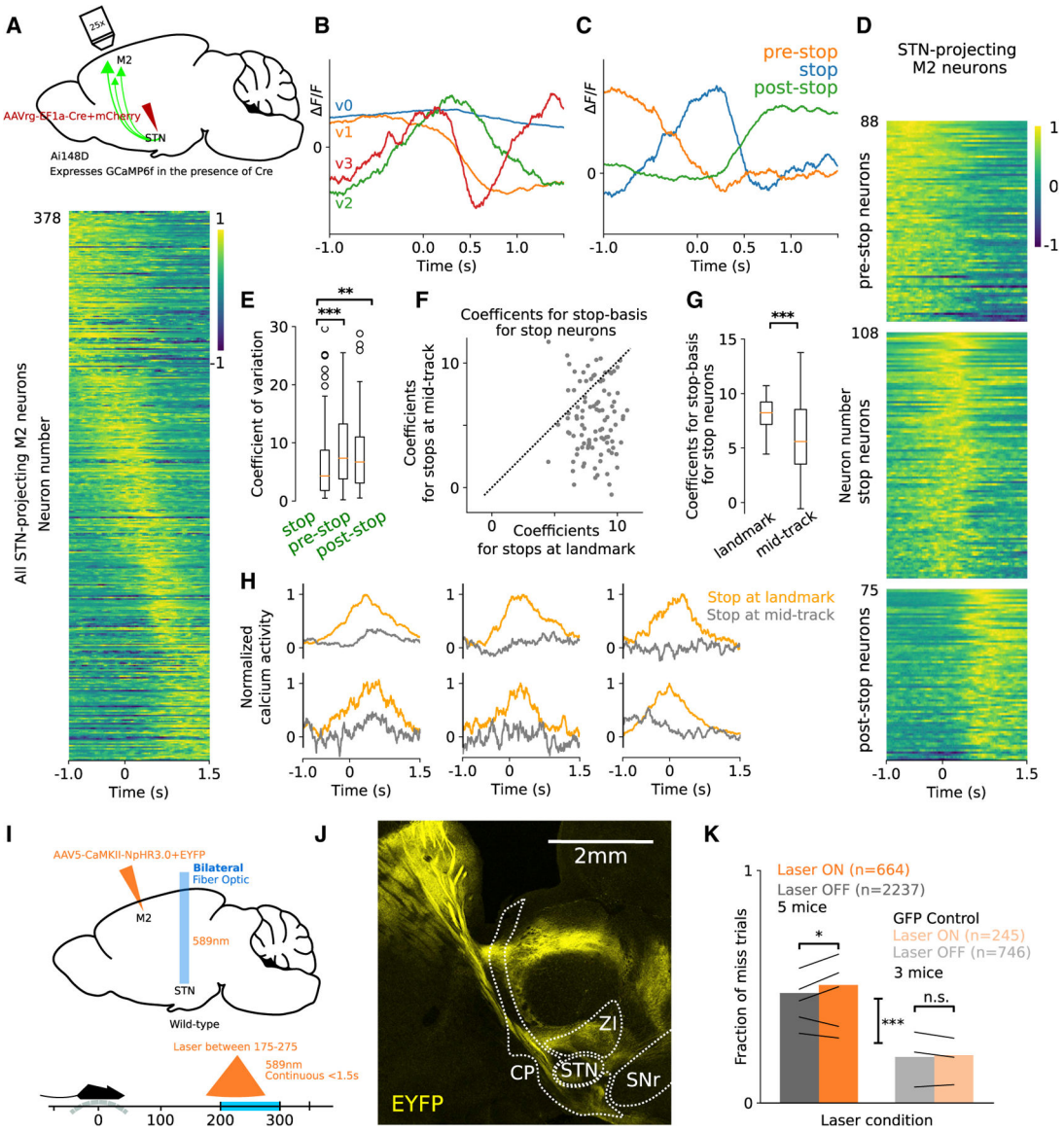

Figure 4. Stop activity is seen in STN-projecting M2 neurons at landmark stops but not at mid-stops

(A) Top: An AAV virus was injected in STN of Ai148D mice (N = 4 mice, applicable to A–H) to retrogradely express Cre, and thereby GCaMP6f in M2 neurons projecting there. Bottom: Plot showing the normalized average calcium activity of labeled M2 neurons within landmark-stop windows aligned to the switching point.

(B) Graph showing a basis for a 4-dimensional subspace that captures >70% of the energy in the responses, all pooled together.

(C) Graph showing 3 templates of ideal neuronal responses, derived through a change of basis from the templates in (B), that are selectively active in different epochs in the task: before stops (pre-stop), during stops (stop), and after stops (post-stop). Each neuronal response can then be expressed as a weighted combination of these 3 templates.

(D) Plot showing neurons (n = 271), whose neural response energy (area under the squared signal) was >80% explained by the subspace, clustered into 3 groups (pre-stop, stop, and post-stop) using the templates in (B).

(E) Boxplots showing the reliability of neuronal responses during the stop period for each of the 3 clustered populations in (D). High reliability is measured by a low coefficient of variation. Stop neurons show a significantly higher reliability compared to pre-stop (Mann-Whitney *U* test, ***p = 6.3e−4 < 0.005) and post-stop neurons (Mann-Whitney *U* test, *p = 0.011 < 0.05).

(F) Scatterplot of the coefficient of contribution of the stop template in (C) in spontaneous stops versus landmark stops. Each data point represents a stop neuron (N = 108) taken from (D), and the coefficient represents the energy of the response along the dimension of the template, obtained by taking the dot product of the calcium response with the stop template. Landmark stops have a higher coefficient than spontaneous stops, indicating that the stop template has a greater contribution to responses during landmark stops.

(G) Boxplots for the distribution of the coefficients in (F). The orange lines represent the respective medians. The means of the distributions are significantly different (paired t test, ***p = 1.09e−6).

(H) Examples of the calcium activity of 6 M2 neurons projecting to STN during stops at the landmark and in the middle of the track. The response for spontaneous stops is normalized to the maximum value of the corresponding response for landmark stops.

(I) An AAV virus expressing NpHR3.0 was bilaterally injected in M2 of wild-type mice (N = 5 mice) and optic fibers were bilaterally implanted over STN to optogenetically target M2 axons in STN. On pseudorandom trials, amber light (589 nm) was presented continuously starting at position 175 for either 1.5 s or until the animal crossed position 275, whichever occurred first.

(J) Sagittal section showing M2-STN projections expressing EYFP and NpHR3.0.

(K) Plot showing the fraction of miss trials (N = 5 mice) during laser on (inhibiting M2-STN axons), during laser off trials (permutation test, *p = 0.045 < 0.05), and during laser off/on trials for control experiments (N = 3 mice) expressing GFP instead of NpHR3.0 (permutation test, ***p = 0.0 < 0.005).

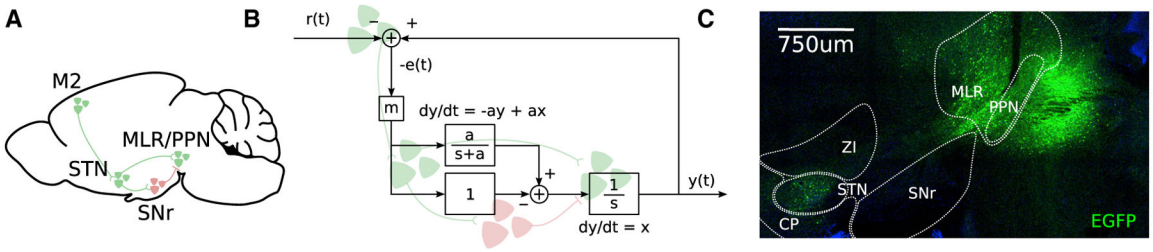

Figure 5. Behavioral dynamics can be physiologically realized through feedback control

(A) Schematic showing the implicated neural circuit, with green and red indicating excitatory and inhibitory cells, respectively. Activity through the corticosubthalamic projection can reach the MLR/PPN either through a direct STN-PPN projection or via an STN-SNr-PPN pathway.

(B) Control theoretic model of corticosubthalamic activity that enables rapid control of locomotion. Each box indicates a transfer function in the Laplace s-domain and is labeled with the corresponding input-output relation, with x, y, and t denoting input, output, and time. The pathways bifurcating from STN interact to simulate mathematical differentiation, canceling the slow integrative dynamics of the PPN.

(C) Sagittal slice showing STN Vglut2+ neurons projecting to PPN. An AAVrg-EF1a-DO_DIO-tdTomato_EGFP virus was injected in PPN of Vglut2-Cre animals (N = 3 mice) to retrogradely express EGFP in Vglut2+ neurons projecting to PPN.

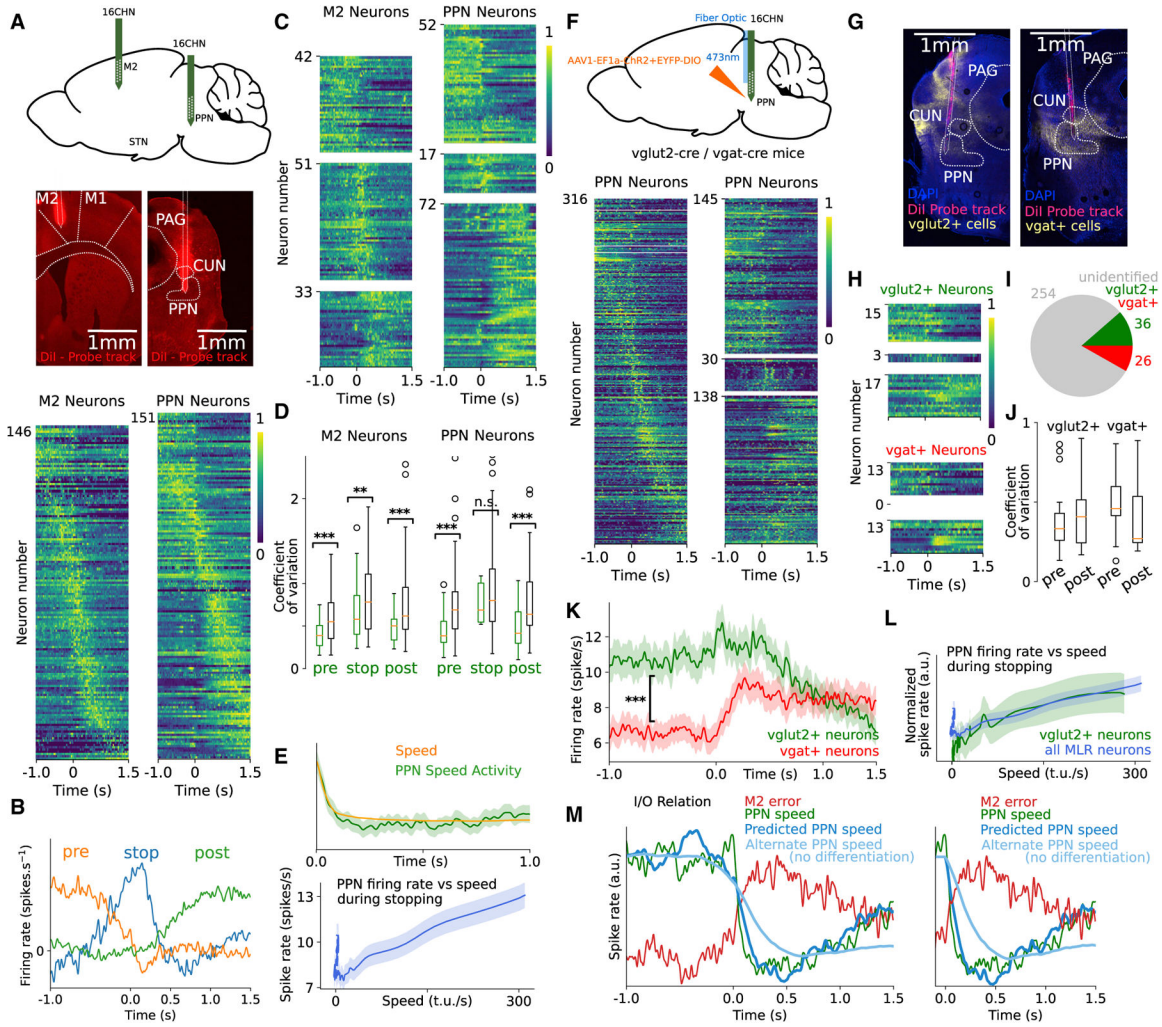

Figure 6. Fast input-output neuronal dynamics are enabled by mathematical differentiation

(A) Top: We recorded extracellular single-unit activity using two 16-channel silicon probes, simultaneously, in M2 and PPN of wild-type mice (N = 4 mice, applicable to A–E).Center: Coronal sections showing DiI recording probe track in M2 and PPN. Bottom: Plot showing the normalized average firing rate of M2 and PPN neurons, within landmark-stop windows aligned to the switching point.

(B) Graph showing 3 templates of ideal neuronal responses related to 3 epochs in the task: pre-stop, stop, and post-stop. Each neuronal response can be expressed as a weighted combination of these 3 templates.

(C) Plots of all of the neurons whose neural response energy (area under the squared signal) was more than 80% explained by the subspace, clustered into 3 groups (pre-stop, stop, and post-stop, from top to bottom) using the templates in (B). The stop-related activity is significantly more prominent in M2 compared to PPN, comprising 40.5% (51 of 126) of the neurons in M2 versus 12.1% (17 of 141) in PPN (chi-square test, $p = 3.5e{-}14 < 0.005$).

(D) Boxplots showing the reliability of neuronal responses during the pre-stop, stop, and post-stop period for M2 and PPN neurons. The reliability of each of the 3 clustered populations in (C) is computed in its corresponding epoch (e.g., the reliability of the pre-stop

cluster is computed at the pre-stop epoch) and compared to that of the remaining neurons. High reliability is measured by a low coefficient of variation. Clustered neurons show increased reliability for their corresponding epoch (Mann-Whitney *U* test, ***p < 0.005, **p < 0.01), with stop PPN neurons showing a non-significant difference from the remaining neurons (Mann-Whitney *U* test, p = 0.329).

(E) Top: Plot superposing the speed of the animal and the speed-related PPN neural response following the switching point. Bottom: Plot showing the speed-related PPN neural response plotted against the speed of the animal, following the switching point. The dashed red line is fit through linear regression to the data during the first second after the switching point (R^2 = 0.829 p = 5.36e−78). Activity in PPN is linearly related to the speed of the animal during locomotion halts (N = 4 mice).

(F) Top: ChR2 was expressed in a Cre-dependent manner in PPN neurons of Vglut2-Cre and Vgat-Cre mice (N = 3 mice for each line, applicable to F–M). An optic fiber coupled with a recording probe was lowered above PPN to identify Vglut2+ and Vgat+ PPN cells expressing ChR2 while recording. Bottom: Plots showing all of the neurons recorded during phototagging and their clustering into 3 clusters as in (C).

(G) Coronal sections showing DiI probe track location and ChR2 expression (mCherry) in Vglut2+ and Vgat+ PPN cells.

(H) Plots showing the 3 clusters of Vglut2+ and Vgat+ identified cells as clustered in (C).

(I) Plot showing the fraction of unidentified, Vglut2+, and Vgat+ cells among all recorded cells, before applying the clustering in (F) and (H).

(J) Boxplots showing the reliability of neuronal responses for pre- and post-stop neurons during the pre- and post-stop epochs, respectively. $Vglut^{2+}$ neurons show higher reliability in pre-stop neurons (Mann-Whitney *U* test, n.s. p = 0.325), while $Vgat^{+}$ cells show higher reliability in post-stop neurons (Mann-Whitney *U* test, n.s. p = 0.129).

(K) Plot showing the average responses of Vglut2+ and Vgat+ neurons, with a significant difference in the pre-stop epoch (Mann-Whitney *U* test, ***p = 1.6e−37 < 0.005).

(L) Plot showing the normalized speed-related PPN neural response of Vglut2+ cells (green) and the cells recorded in (A) (blue) plotted against the speed of the animal, following the switching point. The linear relation observed in (E) extends to Vglut2+ neurons.

(M) Left: Plot showing the reconstructed M2 error signal (input), the PPN response (output), and the predicted PPN response using the reconstructed input-output relation (predicted output) starting from 1 s before the stopping onset. The plot also shows an alternative prediction obtained by removing the STN-PPNprojection from the model, where we find that activity cannot decay quickly enough (RMSE computed starting from the switching point, $RMSE_{alternate}/RMSE_{predicted}$ = 4.45-fold increase). Right: Plot showing the same analysis, but performed starting at the onset of stopping, by forcing the error signal to be zero before time 0, thereby forcing speed decay to initiate only at the onset of stopping ($RMSE_{alternate}/RMSE_{predicted}$ = 6.63-fold increase).

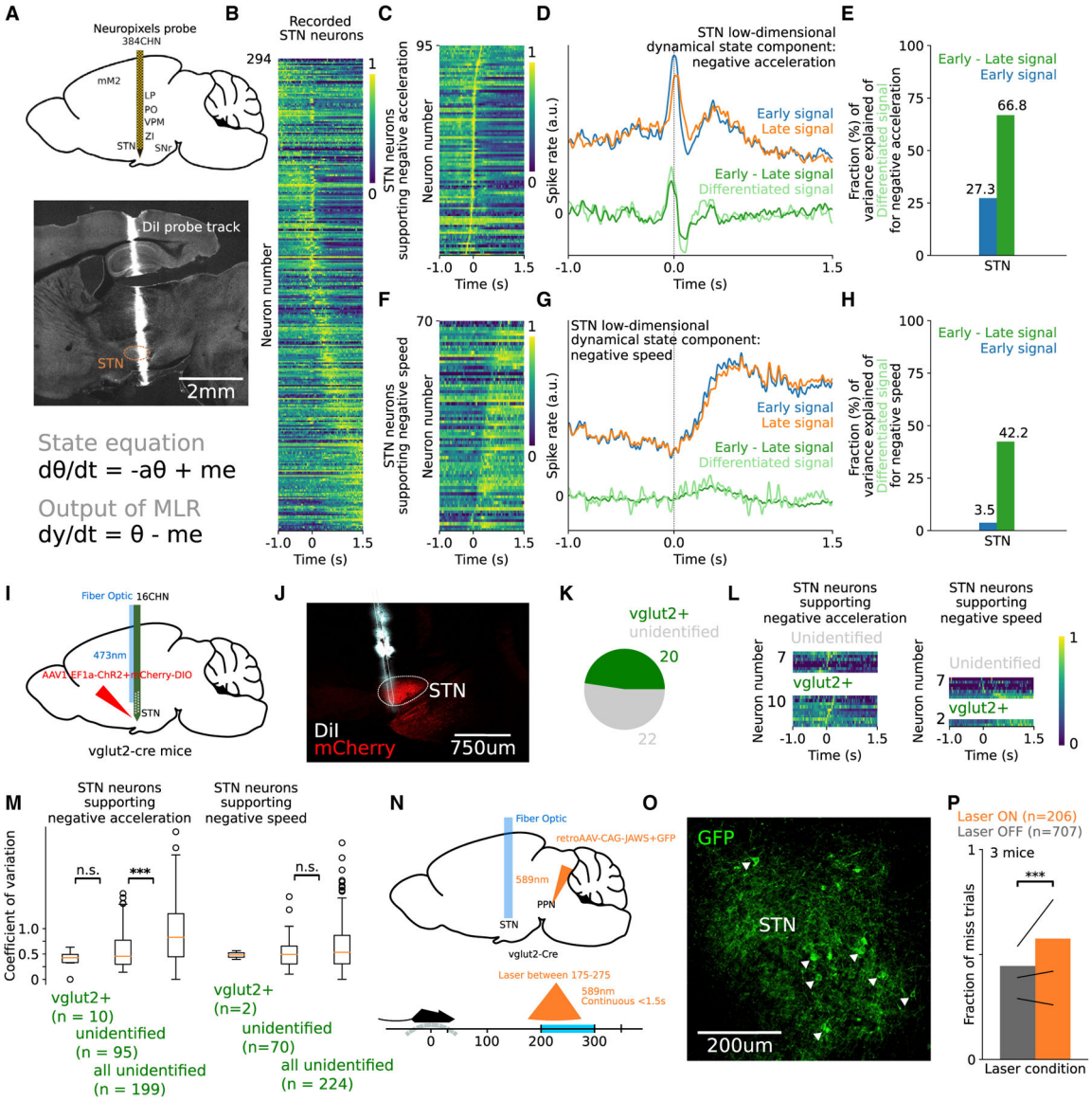

Figure 7. STN supports the dynamical state required to drive the dynamics

(A) Top: We recorded extracellular single-unit activity in the STN of wild-type mice (N = 4 mice, applicable to A–H) using Neuropixels probes. Center: Sagittal section showing the Neuropixels probe placement track (DiI) after recording. Bottom: Equations that dictate the evolution of the dynamical state q, and its interaction with the error signal *e* to produce a differentiated input *y* to PPN. The scaling factors *a* and *m* represent the time constant and gain in the control diagram of Figure 5B.

(B) Plot of the normalized firing rate of STN neurons, within landmark stop windows aligned to the switching point.

(C) Plot showing neurons whose activity peaks between 250 ms and after 250 ms of the stop onset. The neurons are ordered by peak timing.

(D) Within the population of (C), we recreated 2 low-dimensional signals representing the negative acceleration component of the error signal (early signal) and its dynamical state

counterpart (late signal). The difference of these 2 produced a differentiated signal, matching the theoretical prediction.

(E) Bar graph showing the variance of the theoretical differentiated signal in (D) explained by the difference between the early and late signals (green) versus that explained by the early signal as if no computation was performed (blue).

(F) Plot showing neurons whose activity transitions from low to high between 250 ms before the stop onset and 750 ms after.

(G) Within this population of (F), we recreated 2 low-dimensional signals representing the negative speed component of the error signal (early signal) and its dynamical state counterpart (late signal). The difference of these 2 produced a differentiated signal, matching the theoretical prediction.

(H) Bar graph showing the variance of the theoretical differentiated signal in (G) explained by the difference between the early and late signals (green) versus that explained by the early signal as if no computation was performed (blue).

(I) ChR2 was expressed in a Cre-dependent manner in STN neurons of Vglut2-Cre mice (N = 2 mice, applicable to I–L). An optic fiber coupled with a recording probe was lowered above STN to identify STN cells expressing ChR2 while recording.

(J) Sagittal section showing the DiI probe track location and ChR2 expression (mCherry) in Vglut2+ cells in STN.

(K) Plot showing the fraction of $Vglut^{2+}$ identified cells among recorded cells.

(L) Plots showing neuronal responses clustered as in (C) and (F) for the recorded cells.

(M) Boxplots showing the reliability of neuronal responses during the stop period for STN cells supporting negative acceleration and during the post-stop period for STN cells supporting negative speed. $Vglut^{2+}$ cells show a reliability similar to the unidentified cells during the stop period (Mann-Whitney U test, n.s. $p = 0.236$), which show a significant difference in reliability compared to the remaining recorded STN cells, not supporting negative acceleration (Mann-Whitney U test, ***$p = 5.4e{-}7 < 0.005$).

(N) A retroAAV expressing Jaws in a Cre-dependent manner was bilaterally injected in PPN of Vglut2-cre mice (N = 3 mice), and optic fibers were bilaterally implanted over STN to target the Vglut2+ STN neurons projecting to PPN. On pseudorandom trials, amber light (589 nm) was presented continuously starting at position 175 for either 1.5 s or until the animal crosses position 275, whichever occurs first.

(O) Sagittal section showing STN neurons projecting to PPN and retrogradely expressing GFP and Jaws.

(P) Plot showing the fraction of miss trials (N = 3 mice) during laser on and off trials (permutation test, ***$p = 0.004 < 0.005$).

KEY RESOURCES TABLE

REAGENT or RESOURCE	SOURCE	IDENTIFIER
Bacterial and virus strains		
pAAV-CamKIIa-hChR12-(H134R)-mCherry-WPRE-pA	Karl Deisseroth, Stanford University	26975-AAV5; RRID: Addgene_26975
pAAV-Ef1a-mCherry-IRES-Cre	Karl Deisseroth, Stanford University	55632-AAVrg; RRID: Addgene_55632
pAAV-CaMKIIa-eNpHR 3.0-EYFP	Karl Deisseroth, Stanford University	Addgene, 26971-AAV1; RRID: Addgene_26971
(pAAV-CAG-FLEX-rc [Jaws-KGC-GFP-ER2],	(Chuong et al., 2014)	Addgene, 84445-AAVrg; RRID: Addgene_84445
AAV-EF1a-double floxed-hChR2 (H134R)-EYFP-WPRE-HGHpA	Karl Deisseroth, Stanford University	Addgene, 20298-AAV1; RRID: Addgene_20298
pAAV-EF1a-double floxed-hChR2 (H134R)-mCherry-WPRE-HGHpA	Karl Deisseroth, Stanford University	Addgene, 20297-AAV1; RRID: Addgene_20297
pAAV-Ef1a-DO_DIO-TdTomato_EGFP-WPRE-pA	Saunders et al. (2012)	Addgene, 37120-AAVrg; RRID: Addgene_37120
pAAV-CAG-GFP	Edward Boyden, Massachusetts Institute of Technology	Addgene, 37825-AAV1; RRID: Addgene_37825
Chemicals, peptides, and recombinant proteins		
Dil Stain (1,1'-Dioctadecyl-3,3,3',3'-Tetramethylindocarbocyanine Perchlorate	Thermofischer	D282
Experimental models: Organisms/strains		
C57BL/67	Jackson Laboratory	RRID:IMSR_JAX:000664
Ai148(TIT2L-GC6f-ICL-tTA2)-D (or Ai148D)	Jackson Laboratory	RRID:IMSR_JAX:030328
VGlut2-ires-cre knock-in (C57BL/6J)	Jackson Laboratory	RRID:IMSR_JAX:028863
Vgat-ires-cre knock-in (C57BL/6J)	Jackson Laboratory	RRID:IMSR_JAX:028862